Quantitative visualization of two-phase flow in a fractured porous medium

Zhen Liao[1], Russell L Detwiler[2], Esther S Cookson[2], Wanjun Lei[1], and Yi-Feng Chen[3]

[1]State Key Laboratory of Water Resources and Hydropower Engineering Science
[2]University of California, Irvine
[3]Wuhan University

August 14, 2023

Abstract

Two-phase fluid flow in fractured porous media impacts many natural and industrial processes but our understanding of flow dynamics in these systems is constrained by difficulties measuring the flow in the interacting fracture and porous media. We present a novel experimental system that allows quantitative visualization of the air and water phases in a single analog fractured porous medium. The fracture system consists of a sintered-glass porous plate in contact with an impermeable glass plate. A reservoir connected to the porous plate allows control of pore pressure within the porous medium. The fracture fills and drains through the porous matrix and flow manifolds along two edges of the fracture. The fracture is mounted in an imaging system that includes a controlled light-emitting diode (LED) panel and a charge-coupled-device (CCD) camera. Flow and pressure are controlled and monitored by a computer during experiments. To demonstrate this system, we carried out a series of cyclic drainage and imbibition experiments in fractures bounded by porous media with different pore-size distributions in the porous matrix. Images of the drainage process demonstrate that the air-water distribution within the fracture evolves differently than has been observed in non-porous fractured systems. Specifically, we observed limited trapping of water within the fracture during drainage. Conversely, during imbibition, because air cannot exit through the porous matrix, significant regions of air became entrapped once pathways to the fracture boundaries became water filled. The differences in phase evolution led to substantial differences in the evolution of estimated relative permeability with saturation.

Quantitative visualization of two-phase flow in a fractured porous medium

Zhen Liao[1,2], Russell L. Detwiler[3], Esther Cookson[3], Wanjun Lei[1,2], Yi-Feng Chen[1,2]

[1]State Key Laboratory of Water Resources Engineering and Management, Wuhan University, Wuhan 430072, China

[2]Key Laboratory of Rock Mechanics in Hydraulic Structural Engineering of the Ministry of Education, Wuhan University, Wuhan 430072, China

[3]Department of Civil and Environmental Engineering, University of California Irvine, Irvine, CA, United States

Key Points:

- Developed a novel experimental method to visualize two-phase flow in a fracture in a porous matrix.
- The evolution of the air-water distribution within the fracture was measured during sequential drainage and imbibition experiments.
- Capillary head versus saturation curves are sensitive to the pore-size distribution of the bounding porous matrix.

Corresponding author: Russell L. Detwiler, `detwiler@uci.edu`

Abstract

Two-phase fluid flow in fractured porous media impacts many natural and industrial processes but our understanding of flow dynamics in these systems is constrained by difficulties measuring the flow in the interacting fracture and porous media. We present a novel experimental system that allows quantitative visualization of the air and water phases in a single analog fractured porous medium. The fracture system consists of a sintered-glass porous plate in contact with an impermeable glass plate. A reservoir connected to the porous plate allows control of pore pressure within the porous medium. The fracture fills and drains through the porous matrix and flow manifolds along two edges of the fracture. The fracture is mounted in an imaging system that includes a controlled light-emitting diode (LED) panel and a charge-coupled-device (CCD) camera. Flow and pressure are controlled and monitored by a computer during experiments. To demonstrate this system, we carried out a series of cyclic drainage and imbibition experiments in fractures bounded by porous media with different pore-size distributions in the porous matrix. Images of the drainage process demonstrate that the air-water distribution within the fracture evolves differently than has been observed in non-porous fractured systems. Specifically, we observed limited trapping of water within the fracture during drainage. Conversely, during imbibition, because air cannot exit through the porous matrix, significant regions of air became entrapped once pathways to the fracture boundaries became water filled. The differences in phase evolution led to substantial differences in the evolution of estimated relative permeability with saturation.

1 Introduction

Two-phase flow in fractured porous media plays an important role in natural processes such as infiltration into fractured rock and engineered processes such as enhanced oil/gas recovery (Karpyn et al., 2009; Rangel-German & Kovscek, 2002), geological CO_2 sequestration (Vafaie et al., 2023), and remediation of groundwater contaminated by non-aqueous phase liquids (NAPL) (Dearden et al., 2013). Related two-phase flow processes can be broadly categorized as either drainage (non-wetting phase displaces the wetting phase) or imbibition (wetting phase displaces the non-wetting phase).

Early studies of two-phase flow through fractures considered fractures in a non-porous matrix. These studies included experiments in transparent models (e.g., Nicholl et al., 1994; Su et al., 1999) or replicas (e.g., Persoff & Pruess, 1995; Wan et al., 2000) and invasion percolation simulations in variable aperture fields (e.g., Glass et al., 1998; Xu et al., 1998; Yang et al., 2012). In such fractures, flow of the two fluids occurs only through the fracture and the distribution of the phases depends on characteristics of the fracture aperture and the nature and history of the displacement processes. Furthermore, both the wetting and non-wetting fluid may become entrapped and immobilized in regions that are isolated from the fracture boundaries.

When the fractured matrix contains non-negligible porosity, flow of one or both fluids can occur through the fracture and the porous matrix. Two general experimental approaches have been used to study two-phase flow in fractured porous media. The first approach uses micromodels that represent a two-dimensional (2D) cross-section through a fracture; the fracture is a 2D channel and the adjacent porous matrix is a 2D slice of porous medium (e.g., Haghighi et al., 1994; Wan et al., 1996; Rangel-German & Kovscek, 2006). Such experimental systems allow direct visualization of the interaction of multiple phases within the fracture and porous matrix, but neglect the 3D interaction of the phases within the fracture induced by aperture variability.

The second approach combines two-phase flow through cores of fractured porous rock with X-ray computed tomography to observe the distribution of phases within the fracture and porous matrix (Rangel-German & Kovscek, 2002; Karpyn et al., 2009; Arshadi et al., 2018). This has the advantage of providing measurements of the distribution of two or more phases within the pore space (both fracture and porous matrix) in fractured cores. However, the temporal and spatial resolution of CT scans constrains the scalability of these studies. For example, Arshadi et al. (2018) imaged 5-mm segments of a larger fractured core at a 2.5-μm voxel resolution. Such high spatial resolution facilitates identification of phases within pores in the matrix, but limits the size of the fracture that can be imaged.

We developed a novel fractured porous media experimental test cell that consists of a translucent porous glass surface mated with a transparent non-porous glass surface. Quantitative visualization techniques facilitate direct measurement of the evolving phase distribution within the 15$\times$15-cm fracture at a spatial resolution of ~ 75 μm and a temporal resolution of ~ 1 Hz. We demonstrate the new system through a series of drainage and imbibition experiments in fractures with two different pore-size distributions in the porous matrix. We details the experimental system and fabrication of the fracture model in Section 2 ; Section 3 describes the experimental procedure used to demonstrate the results along with the required data analyses; Section 4 presents the results of the demonstration experiments; and Section 5 provides concluding remarks.

2 Experimental System

The experimental system (Figure 1a) includes a test stand that rigidly supports a 12-bit CCD camera (Quantix KAF-6303e; 2048×3072 pixels), red LED backlight panel (with an emitted wavelength of ∼625 nm) and the experimental model. The test stand can rotate from −90° to 90° so gravitational forces acting on the fluid in the fracture can be varied. The spatial resolution of images of the fracture plane was 75 × 75 μm. Opaque fabric covers the test stand to minimize stray light in the imaging system. Similar experimental systems have been used to study a range of flow and transport processes in single variable aperture fractures (e.g., Nicholl et al., 1999; Detwiler et al., 1999, 2002)

[Figure 1 about here.]

In this study, we have developed a novel fracture test cell that includes a porous fracture surface. Figure 1b shows a schematic of the fractured porous medium test cell. A porous glass plate (bottom) mated with a smooth glass plate (top) served as the 15×15-cm fracture surfaces. A unique feature of this configuration is that the bottom porous surface is both permeable and translucent, so transmitted light can be measured during experiments. Thus, changes in measured transmitted light intensity reflect the evolving distribution of air and water within the fracture (see Section 3.2 for details). Furthermore, using porous glass with different pore sizes provides the opportunity to directly quantify the influence of matrix porosity and permeability on two-phase flow processes in fractured porous media. The example experiments presented here used two different pieces of porous glass surfaces (Rudong Shundao Glass Instrument Factory, China) with reported pore-size distributions of 4-7 μm (FF - fracture with fine pore-size matrix) and 16-30 μm (MF - fracture with medium pore-size matrix).

Two 1.9-cm-thick fused-quartz windows supported by aluminum frames enclosed the fracture surfaces. Clear polyvinyl chloride (PVC) gaskets separated each fracture surface from the fused-quartz window creating empty cavities between each fracture surface and the supporting window. A needle through the gasket into the lower cavity provided an inlet/outlet for water flow in/out of the porous matrix. To prevent leakage from the edges of the porous lower surface, a rim of dyed epoxy was applied along the peripheral edges of the porous glass (see Text S1, Figure S1 and Figure S2 for additional details).

After placing the smooth glass and the porous glass surfaces in contact to create the fracture, normal stress was applied to the frame by tightening the connecting bolts to a uniform torque (typically 1.7 N·m). Figure 1b shows a rigid frame surrounding the fracture with bolts that apply force to the no-flow boundaries (left and right sides) and flow manifolds (top and bottom). The flow manifold has a $\sim$3 $\times$ 5-mm channel along the entire width of the fracture to ensure that pressure gradients along the manifold channel are negligible relative to pressure gradients within the fracture.

Fluid entered and exited the fracture through tubing connected to the cavity needle and the flow manifolds. For the experiments presented here, a Marriotte bottle connected to the cavity needle served to control the head in the permeable matrix (bottom fracture surface). The Marriotte bottle was positioned on an analytical balance (Mettler Toledo MS4002S/03) on a variable-height stage, which allowed reproducible head changes of up to $\pm$ 70 cm relative to the middle of the fracture plane. We define the capillary head as:

$$\Psi = \frac{p_\mathrm{a} - p_\mathrm{w}}{\rho_\mathrm{w} g} = \frac{p_\mathrm{c}}{\rho_\mathrm{w} g} \tag{1}$$

where p_a, p_w, and p_c are the atmospheric, water, and capillary pressure, respectively, ρ_w is the density of water and g is acceleration due to gravity. During all experiments, a pressure transducer (Validyne DP15-42) monitored p_w at 0.167 Hz. Mass flow rate in and out of the fracture was recorded by the analytical balance. A computer connected to the experimental system controlled data acquisition from each of the sensors (camera, pressure transducer, and balance) using Labview (e.g., Bitter et al., 2006). Manometers adjacent to the pressure transducer facilitated periodic calibration of the pressure transducer but were isolated from the fracture during drainage and imbibition experiments. Because Marriotte bottles lead to small pressure oscillations when bubbles release from the vent tube, we terminated the vent tube with a 16-gauge needle and applied a 0.4 atm vacuum to the head space in the bottle. This caused a steady stream of bubbles from the vent tube and negligible pressure oscillations. To minimize evaporation losses from the Marriotte bottle, we humidified the vent air entering the bottle (Figure 1).

3 Cyclic Drainage and Imbibition Experiments

To demonstrate the capabilities of this new experimental system, we carried out several cyclic drainage and imbibition experiments. Horizontal experiments were carried out in the MF and FF models (Experiments MFH and FFH, respectively) to investigate the effect of the matrix permeability, and one vertical experiment was conducted in FF model (Experiment FFV) to explore the added effect of gravity. Note, results from MFH and FFH are discussed in Section 4; the results of FFV are included in the Supplementary Information (Text SS5).

3.1 Experimental Procedure

Each experimental sequence involved: primary drainage → primary imbibition → secondary drainage → secondary imbibition. Before each experiment, carbon dioxide was injected through the cavity, porous matrix and dry fracture to displace air from the test cell. Then deionized, de-aired water was injected to saturate the fracture. Prior to initializing the first drainage sequence, the boundary conditions for the fracture were established. For the horizontal experiments, the flow manifolds and all connected tubing were drained so the manifolds were filled with air at atmospheric pressure. For the vertical experiment, the top flow manifold and connected tubing were drained, establishing a zero-pressure, air boundary at the top of the fracture, while the bottom manifold and connected tubing were valved off, establishing a no-flow boundary at the bottom of the fracture.

The drainage-imbibition cycles were conducted by sequentially varying the capillary head in the cavity through a set of static displacements of the Marriotte bottle. Image acquisition began before initially changing the position of the Marriotte bottle and continued until the final drainage or imibibition step. During each step, the valve between the cavity and Marriotte bottle (E) was closed as the height of the bottle was adjusted. The valve was then opened and the fracture was allowed to drain or fill until equilibrium. We determined when equilibrium was reached by observing differences between successive raw images and differences between successive mass readings from the digital balance recording the mass of the Marriotte bottle. Each drainage-imbibition cycle was completed during a single day followed by an approximately 12-hour pause before completing the secondary drainage-imbibition cycle.

3.2 Measurement of Evolving Phase Distribution

To aid interpretation of the images acquired during experiments, we developed an image processing script in MATLAB to convert raw images to binary images that distinguished the two phases (air / water). Figure 2 shows the steps of the image processing procedure. At the start of each experiment, we took a sequence of 100 reference images of the saturated matrix and fracture, which we averaged to yield a single, low-noise reference image (Figure 2a). To account for nonuniformities in light transmission through the porous matrix and fracture, we normalized each experimental image (Figure 2b) by the reference image. The natural logarithm of the resulting normalized field quantifies light absorbance at each pixel (Figure 2c).

[Figure 2 about here.]

Light scattering at the interface between the porous matrix and the fracture complicates differentiating air and water within the fracture. Rather than a sharp edge, the air-water interface appears in the absorbance field as a diffuse zone where the values transition from near zero for water to approximately 0.2 for air (Figure 2c). To quantify the location of the interface, we sought a global threshold that minimized the number of air clusters during the primary drainage cycle. The rationale for this approach is that, during primary drainage, we expect the formation of a connected air cluster originating from the fracture inlet with minimal fragmenting of this cluster until the beginning of the subsequent imbibition cycle. Due to noise in the images, smaller threshold values cause localized water-filled regions to be misidentified as air resulting in an increase in the number of air-filled clusters. Larger threshold values cause some thin air-filled channels to be misidentified, separating the large invading cluster into multiple clusters.

To determine the global absorbance threshold, we developed an algorithm that sequentially incremented the threshold over a range that included the likely global threshold value, binarized the field according to each threshold value and counted the resulting number of discrete air clusters. We repeated this process for each image during the primary drainage cycle. Plotting the average number of segmented air clusters, N_{ave}, versus the threshold values for experiments FFH and FFV, T_{FFH} and T_{FFV}, reveals distinct minima for these curves. The respective optimal threshold, $T^{\star}$ for these two experiments were $T^{\star}_{\mathrm{FFH}}$=0.083 and $T^{\star}_{\mathrm{FFV}}$=0.105. We selected a global value of $T^{\star} = 0.094 \pm 0.014$ (average from the two experiments ± 15%) Figure 2d) as the optimal threshold. Figure 2e and f show the results of binarizing using the upper and lower bounds for $T^{\star}$ ($T^{\star}_{\mathrm{lb}} =$ 0.08 and $T^{\star}_{\mathrm{ub}} = 0.108$) and demonstrate that the most significant discrepancies occur where thin tendrils of water (black phase) connect two larger regions of water. We consider the range of possible interface locations as a source of uncertainty in calculations of saturation presented in Section 4. For Experiment MFH, the optimal threshold was $T^{\star}_{\mathrm{MFH}} =$ 0.042 ± 0.006 (Figure S3).

4 Experimental results

Images acquired during each experiment allow us to quantify the evolving phase distribution within the fracture. Figure 3 compares the primary and secondary drainage and imbibition cycles for horizontal experiments in the FF and MF fractures. The colors reflect air occupancy at sequential values of Ψ during each step of the experiment, with warm colors indicating smaller Ψ and cool colors indicating larger Ψ; black regions remained water-filled for all Ψ. The grey regions in the secondary drainage figures are regions that remained air-filled at the end of primary imbibition.

[Figure 3 about here.]

For both experiments, air entered the fracture only after Ψ exceeded the air entry pressure of the fracture ($\Psi_{\mathrm{a,e}}$). Initial air entry occurred after the step from $\Psi = 274$ mm to 325 mm for FFH and after the step from $\Psi = 174$ mm to 190 mm for MFH. The different values of $\Psi_{\mathrm{a,e}}$ reflect differences in the fracture aperture along the two flow boundaries for the two experiments. Though the nonporous glass surface and porous matrix were placed in contact to create the fractures, the size of the sintered beads used to create MF were larger than those used for FF (Figure S4), resulting in a larger aperture and lower $\Psi_{\mathrm{a,e}}$ for MF. The Laplace-Young relationship relates $\Psi_{\mathrm{a,e}}$ to the corresponding fracture apertures (see supporting information Text SS4 and Figure S5 for details) and suggests that the apertures along the flow boundaries are between 43 and 50 μm for FF and between 71 and 77 μm for MF.

The binarized distributions of air and water within the fracture at each increment of Ψ (Figure 3) allow us to quantify the areal fraction of the fracture occupied by water, $S_{\mathrm{w}}^{\mathrm{A}}$. This serves as a surrogate for volumetric water saturation, which we cannot precisely quantify because we have only estimates of the fracture aperture and not aperture variability within the fracture. Figures 4a and 4b show Ψ plotted against $S_{\mathrm{w}}^{\mathrm{A}}$ for each cycle of Experiments FFH and MFH, respectively. The Ψ versus $S_{\mathrm{w}}^{\mathrm{A}}$ plots exhibit significant hysteresis, which can be understood by comparing the phase distributions during different cycles of each experiment.

[Figure 4 about here.]

As primary drainage proceeded through sequential steps of Ψ, air entered regions of progressively smaller aperture. For both FFH and MFH, the air first filled regions near the air-filled flow manifolds and then advanced through the center of the fracture until it connected the two manifolds. Then, with further decreases in Ψ, the region occupied by air expanded towards the no-flow boundaries. The similarity in the large-scale displacement pattern in both experiments likely reflects the influence of the clamping pressure applied to the aluminum frames during fracture assembly (Section 2), which leads to smaller apertures around the perimeter of the fracture. The small-scale features of the displacement patterns differ for the two experiments, likely due to the difference in the porous matrix, which influences the magnitude and variability of fracture aperture and matrix permeability.

A common feature of both experiments is the relative absence of regions of trapped water within the drained region of the fractures (i.e., isolated black regions surrounded by colored regions in Figure 3). This differs from experimental observations in fractures bounded by non-porous, impermeable surfaces, where regions of the draining phase become disconnected from the fracture edges and entrapped within the fracture (e.g., Detwiler et al., 2002; Chen et al., 2017). Here, water regions that become isolated during drainage eventually drain through the porous matrix if the aperture is large enough that Ψ exceeds the local air entry pressure in the fracture.

During primary imbibition, water fills the smallest aperture regions along the no-flow edges of the fractures first and then gradually advances towards the center of the fracture with each increment of Ψ. After water filled the fracture along the two flow manifolds, the remaining air became entrapped and immobilized (dark red regions in second row from top in Figure 3). In contrast to the drainage process, the trapping observed during imbibition is similar to that observed in fractures bounded by non-porous, impermeable surfaces. As a result, potentially large regions of air may become entrapped regardless of the presence of secondary porosity in the bounding porous matrix.

During secondary drainage (DR2) in FFH, air spreads more readily through the fracture than during DR1 due to the regions of trapped air remaining after IMB1. The result is that similar distributions of air and water within the fracture occur at lower values of Ψ during DR2 than DR1. This can be observed in Figure 3 where the distributions of air-filled regions at Ψ=398 mm in DR1 is similar to Ψ=374 mm in DR2. Likewise the distribution of air-filled regions at Ψ=423 mm in DR1 is similar to Ψ=398 mm in DR2. Note, this history dependence is not observed for the imbibition cycles, where the initial distribution of air within the fracture was almost identical for IMB1 and IMB2, resulting in a nearly identical filling order (Figure 3). Similar behavior was observed in MFH, but because the drainage process occurred over a narrower range of Ψ, the differences between DR1 and DR2 are less pronounced.

In addition to the smaller $\Psi_{\mathrm{a,e}}$ during primary drainage for the horizontal experiment in Model MF (Experiment MFH, Figure 4), another significant difference between FFH and MFH was the distribution of the air and water phases during each sequence. Specifically, the air clusters in MFH are more compact with less roughness of the air-water interfaces. Previous scaling analyses of two-phase displacements in fractures between non-porous matrices suggest a reasonable explanation for this behavior (Glass et al., 1998, 2003). The competition between interfacial curvature in the fracture plane and across the fracture aperture have been shown to control the geometry of the air-water interfaces; smaller fracture apertures with more aperture variability lead to more tortuous interfaces than larger aperture fractures with less aperture variability.

Glass et al. (2003) derived the dimensionless parameter, $C/\delta = \frac{\langle b \rangle^2}{\sigma_b \lambda_b}$, where C is the dimensionless curvature number, a ratio of in-plane to out-of-plane interfacial curvature, δ is the coefficient of variation of the fracture aperture, and $\langle b \rangle$, σ_b, and λ_b are the mean, standard deviation, and correlation length of the aperture field. They showed that small C/δ led to tortuous air-water interfaces and as C/δ became larger entrapped regions of air became more compact. Though we cannot directly quantify C/δ for our experiments, the air-entry apertures provide an estimate of $\langle b \rangle$. Because the aperture variability in our fractures are induced by the pore-scale variations of the porous surface, both σ_b and λ_b likely scale with the respective pore sizes of the porous plates. Because the maximum pore sizes for MF are approximately 4 times larger than those in FF, this suggests that C/δ is an order of magnitude larger for MF than for FF. This likely explains the difference in the structure of the air-water interfaces for the two experimental sequences.

It is not possible to directly measure the relative permeability of the air and water phases during our experiments, but we can estimate these values through numerical simulations in the measured air-water distributions. For these simulations, we considered only the influence of the geometry of the air and water on estimated relative permeabilities. Detwiler et al. (2005) showed that the role of aperture variability on estimates of fracture relative permeability were minor relative to the distribution of the flowing phases within the fracture. We used the local cubic law to simulate flow of both air and water through the fracture for each value of Ψ represented in Experiments FFH and MFH. Figures 4c and 4d show the relationship between the estimated water and air relative permeabilities, $k_{\mathrm{r,w}}$ and $k_{\mathrm{r,a}}$, respectively, and the areal saturation $S_{\mathrm{w}}^{\mathrm{A}}$ of the water phase.

The relative permeability curves (Figures 4c and 4d) are qualitatively similar to what has been measured in both porous and fractured media in other studies, suggesting the potential utility of empirical permeability-saturation relationships for modeling flow through fractured porous media. However, the potential for the development of fracture-spanning regions of either air or water can strongly influence the evolution of $k_{\mathrm{r,w}}$. This is most notable in comparing $k_{\mathrm{r,w}}$ during primary and secondary drainage for FFH and MFH. The large region of air that forms at the entrance to FFH (Figure 3) caused a significant decrease in $k_{\mathrm{r,w}}$ once $\Psi_{\mathrm{a,e}}$ was exceeded. Conversely, in MFH, the more compact shape of the evolving air region led to a more gradual decrease in $k_{\mathrm{r,w}}$.

5 Concluding Remarks

We have presented the development and evaluation of a new experimental system for exploring two-phase flow processes in porous fractured media. Use of light transmission through the translucent porous fracture surface allows us to quantitatively delineate the distribution of the evolving air-water interface within the fracture. Example experiments in two different fractures demonstrated the role of changing pore pressure in the porous matrix on the distribution of air and water within the fracture, which exhibited significant hysteresis from the primary drainage through subsequent drainage cycles

The primary advantage of this method over other approaches (e.g., 2D micromodels with a channel bounded by a porous matrix or X-ray CT in rock cores) is the ability to resolve the distribution of air and water within a fractured porous medium at: (i) spatial scales that are much larger than the scale of aperture variability and the resulting regions of entrapped phases during displacement processes; and (ii) temporal scales with the potential to resolve potentially rapidly evolving interfacial dynamics. In addition, the demonstration experiments presented here used a smooth glass plate as the upper fracture surface, but such experiments can be readily extended to include a rough upper fracture surface to explore the relative importance of fracture-matrix interactions and two-phase flow processes within a bounding variable aperture fracture.

6 Open Research

All experimental data and processing algorithms required to reproduce the results presented here are publicly available (Liao et al., 2023).

Acknowledgments

The first author was supported by the scholarship under the State Scholarship Fund from the China Scholarship Council for his visit to University of California, Irvine (CSC student number: 201906270102). We also gratefully acknowledge the financial support from the the Basic Science Center Program for Multiphase Media Evolution in Hypergravity of the National Natural Science Foundation of China (No. 51988101), and the National Natural Science Foundation of China (No. 51925906).

References

Arshadi, M., Khishvand, M., Aghaei, A., Piri, M., & Al-Muntasheri, G. A. (2018). Pore-scale experimental investigation of two-phase flow through fractured porous media. *Water Resources Research*, *54*(5), 3602-3631. doi: https://doi.org/10.1029/2018WR022540

Bitter, R., Mohiuddin, T., & Nawrocki, M. (2006). *Labview: Advanced programming techniques*. CRC Press.

Chen, Y., Fang, S., Wu, D., & Hu, R. (2017). Visualizing and quantifying the crossover from capillary fingering to viscous fingering in a rough fracture. *Water Resources Research*, *53*(9), 7756-7772.

Dearden, R., Noy, D., Lelliott, M., Wilson, R., & Wealthall, G. (2013, oct). Release of contaminants from a heterogeneously fractured low permeability unit underlying a DNAPL source zone. *Journal of Contaminant Hydrology*, *153*, 141–155. doi: 10.1016/j.jconhyd.2011.05.006

Detwiler, R. L., Pringle, S. E., & Glass, R. J. (1999). Measurement of fracture aperture fields using transmitted light: An evaluation of measurement errors and their influence on simulations of flow and transport through a single fracture. *Water Resources Research*, *35*(9), 2605-2617. doi: https://doi.org/10.1029/1999WR900164

Detwiler, R. L., Rajaram, H., & Glass, R. J. (2002). Experimental and simulated solute transport in a partially-saturated, variable-aperture fracture. *Geophysical Research Letters*, *29*(8), 113–1–113–4. doi: https://doi.org/10.1029/2001GL013508

Detwiler, R. L., Rajaram, H., & Glass, R. J. (2005). Satiated relative permeability of variable-aperture fractures. *Physical Review E*, *71*, 031114. doi: https://doi.org/10.1103/PhysRevE.71.031114

Glass, R. J., Nicholl, M. J., & Yarrington, L. (1998). A modified invasion percolation model for low-capillary number immiscible displacements in horizontal rough-walled fractures: Influence of local in-plane curvature. *Water Resources Research*, *34*(12), 3215-3234. doi: https://doi.org/10.1029/98WR02224

Glass, R. J., Rajaram, H., & Detwiler, R. L. (2003). Immiscible displacements in rough-walled fractures: Competition between roughening by random aperture variations and smoothing by in-plane curvature. *Physical Review E*, *68*(6), 061110. doi: https://doi.org/10.1103/PhysRevE.68.061110

Haghighi, M., Xu, B., & Yortsos, Y. C. (1994). Visualization and simulation of immiscible displacement in fractured systems using micromodels: I. Drainage. *Journal of Colloid and Interface Science*, *166*(1), 168-179. doi: https://doi.org/10.1006/jcis.1994.1283

Karpyn, Z. T., Halleck, P. M., & Grader, A. S. (2009). An experimental study of spontaneous imbibition in fractured sandstone with contrasting sedimentary layers. *Journal of Petroleum Science and Engineering*, *67*(1), 48-56. doi: https://doi.org/10.1016/j.petrol.2009.02.014

Liao, Z., Detwiler, R. L., Cookson, E. S., Lei, W., & Chen, Y. (2023). *Dataset for: Quantitative visualization or two-phase flo in a fracture porous medium* [dataset]. doi: 10.5281/zenodo.8188007

Nicholl, M. J., Glass, R. J., & Wheatcraft, S. W. (1994). Gravity-driven infiltration instability in initially dry nonhorizontal fractures. *Water Resources Research*, *30*(9), 2533-2546. doi: https://doi.org/10.1029/94WR00164

Nicholl, M. J., Rajaram, H., Glass, R. J., & Detwiler, R. (1999). Saturated flow in a single fracture: evaluation of the reynolds equation in measured aperture fields. *Water Resources Research*, *35*(11), 3361-3373. doi: https://doi.org/10.1029/1999WR900241

Persoff, P., & Pruess, K. (1995). Two-phase flow visualization and relative permeability measurement in natural rough-walled rock fractures. *Water Resources Research*, *31*(5), 1175-1186. doi: https://doi.org/10.1029/95WR00171

Rangel-German, E. R., & Kovscek, A. R. (2002). Experimental and analytical study of multidimensional imbibition in fractured porous media. *Journal of Petroleum Science and Engineering*, *36*(1), 45-60. doi: https://doi.org/10.1016/S0920-4105(02)00250-4

Rangel-German, E. R., & Kovscek, A. R. (2006). A micromodel investigation of two-phase matrix-fracture transfer mechanisms [Journal Article]. *Water Resources Research*, *42*(3). Retrieved from `https://doi.org/10.1029/2004WR003918` (https://doi.org/10.1029/2004WR003918) doi: https://doi.org/10.1029/2004WR003918

Su, G. W., Geller, J. T., Pruess, K., & Wen, F. (1999). Experimental studies of water seepage and intermittent flow in unsaturated, rough-walled fractures.

Water Resources Research, *35*(4), 1019-1037. doi: https://doi.org/10.1029/1998WR900127

Vafaie, A., Cama, J., Soler, J. M., Kivi, I. R., & Vilarrasa, V. (2023, may). Chemo-hydro-mechanical effects of CO2 injection on reservoir and seal rocks: A review on laboratory experiments. *Renewable and Sustainable Energy Reviews*, *178*, 113270. doi: 10.1016/j.rser.2023.113270

Wan, J., Tokunaga, T. K., Orr, T. R., O'Neill, J., & Connors, R. W. (2000). Glass casts of rock fracture surfaces: A new tool for studying flow and transport. *Water Resources Research*, *36*(1), 355-360. doi: https://doi.org/10.1029/1999WR900289

Wan, J., Tokunaga, T. K., Tsang, C.-F., & Bodvarsson, G. S. (1996). Improved glass micromodel methods for studies of flow and transport in fractured porous media. *Water Resources Research*, *32*(7), 1955-1964. doi: https://doi.org/10.1029/96WR00755

Xu, B., Yortsos, Y. C., & Salin, D. (1998). Invasion percolation with viscous forces. *Physical Review E*, *57*, 739–751. doi: https://doi.org/10.1103/PhysRevE.57.739

Yang, Z., Niemi, A., Fagerlund, F., & Illangasekare, T. (2012). A generalized approach for estimation of in-plane curvature in invasion percolation models for drainage in fractures. *Water Resources Research*, *48*(9), W09507. doi: https://doi.org/10.1029/2012WR011829

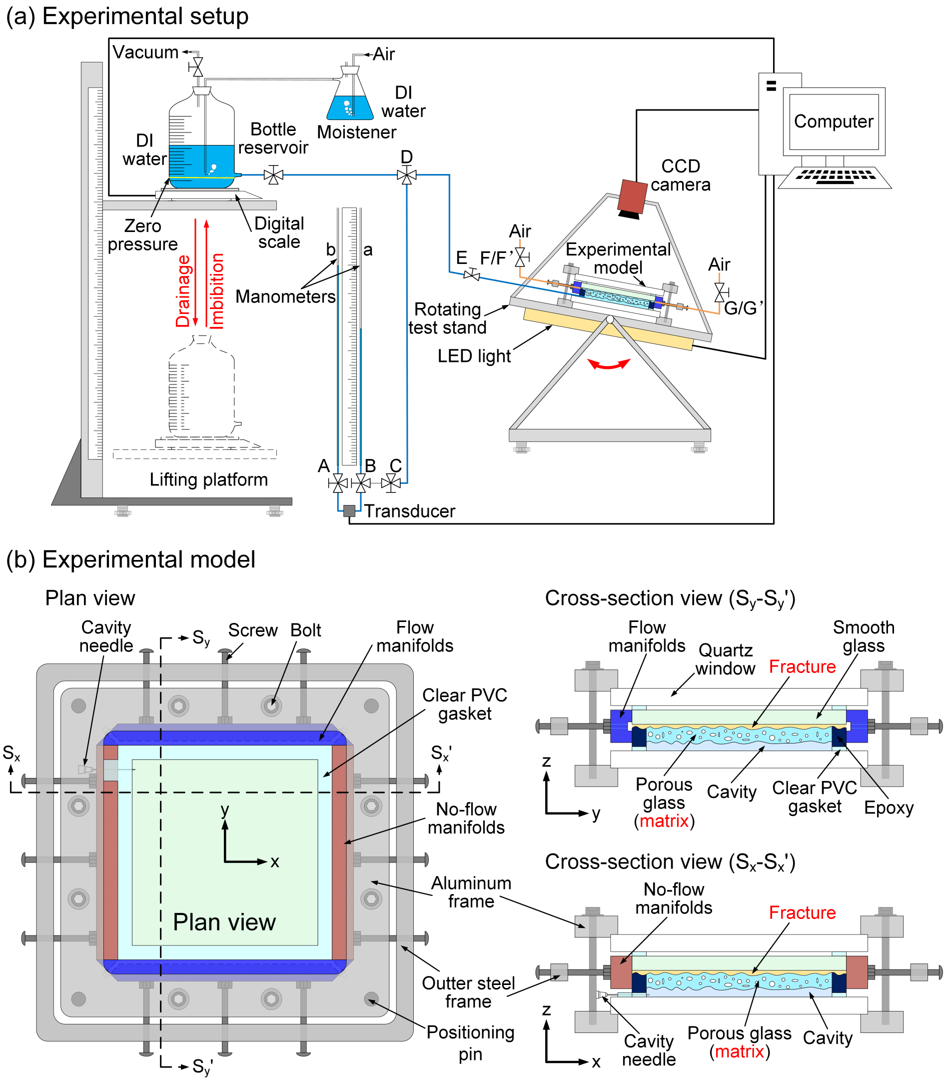

Figure 1. Schematic of experimental system including: (a) an overview of the experimental setup and (b) a plan view and cross-sections of the fracture test cell.

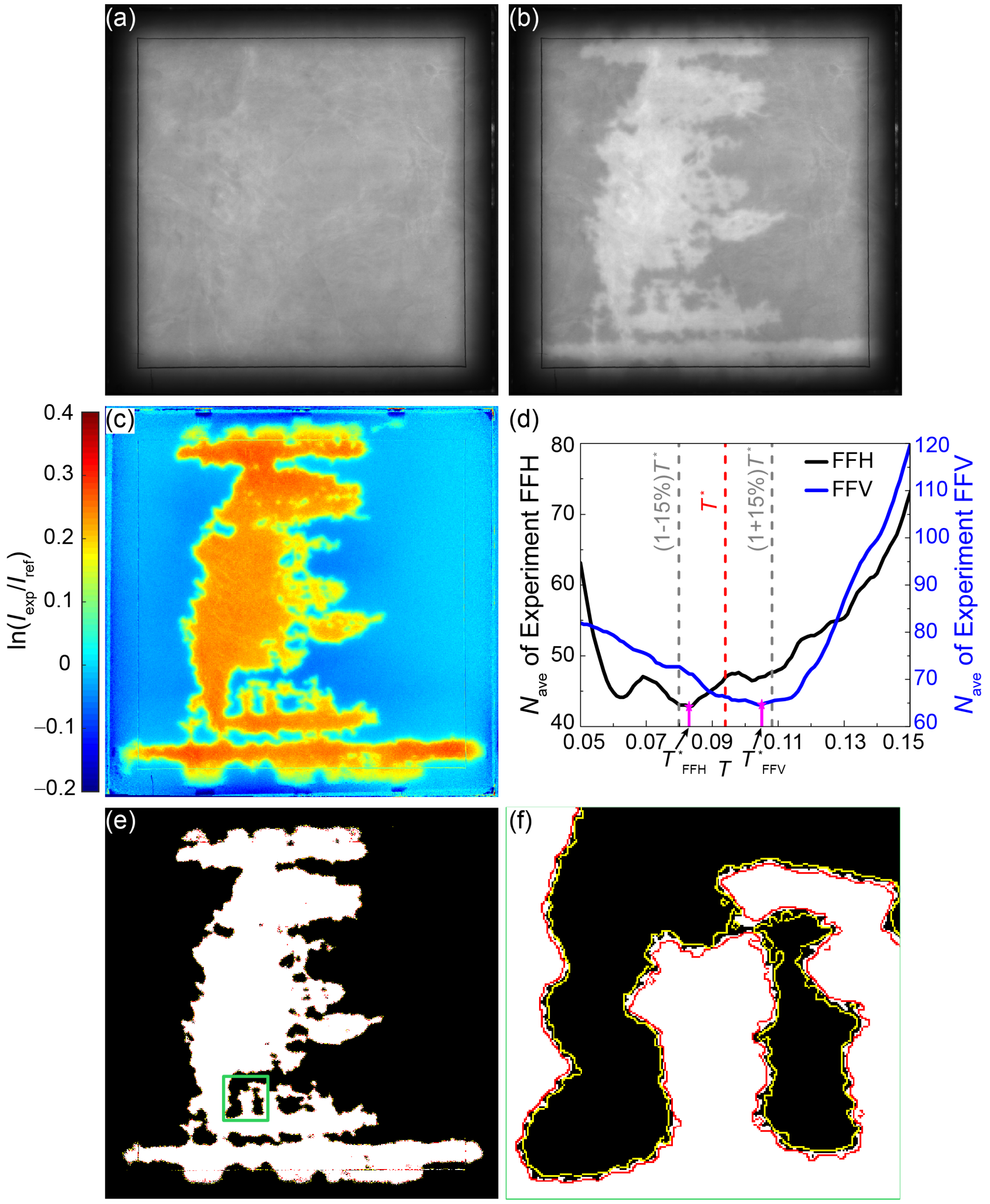

Figure 2. Overview of the image processing procedure, including: (a) The raw grayscale reference image, I_{ref} ; (b) an example of a raw grayscale experimental image, I_{exp}; (c) the corresponding light absorbance field, $A = \ln(I_{\mathrm{exp}}/I_{\mathrm{ref}}$; (d) the relationship between the average number of segmented air clusters, N_{ave}, and the segmenting threshold values for Experiments FFH and FFV, T_{FFH} and T_{FFV}, revealing distinct minima for these curves; (e) the resulting binary image (black - water, white - air) determined using the global threshold with results using the upper and lower bounds of the global threshold indicated by yellow and red lines, respectively; (f) enlarged view of region indicated by the green box in (e).

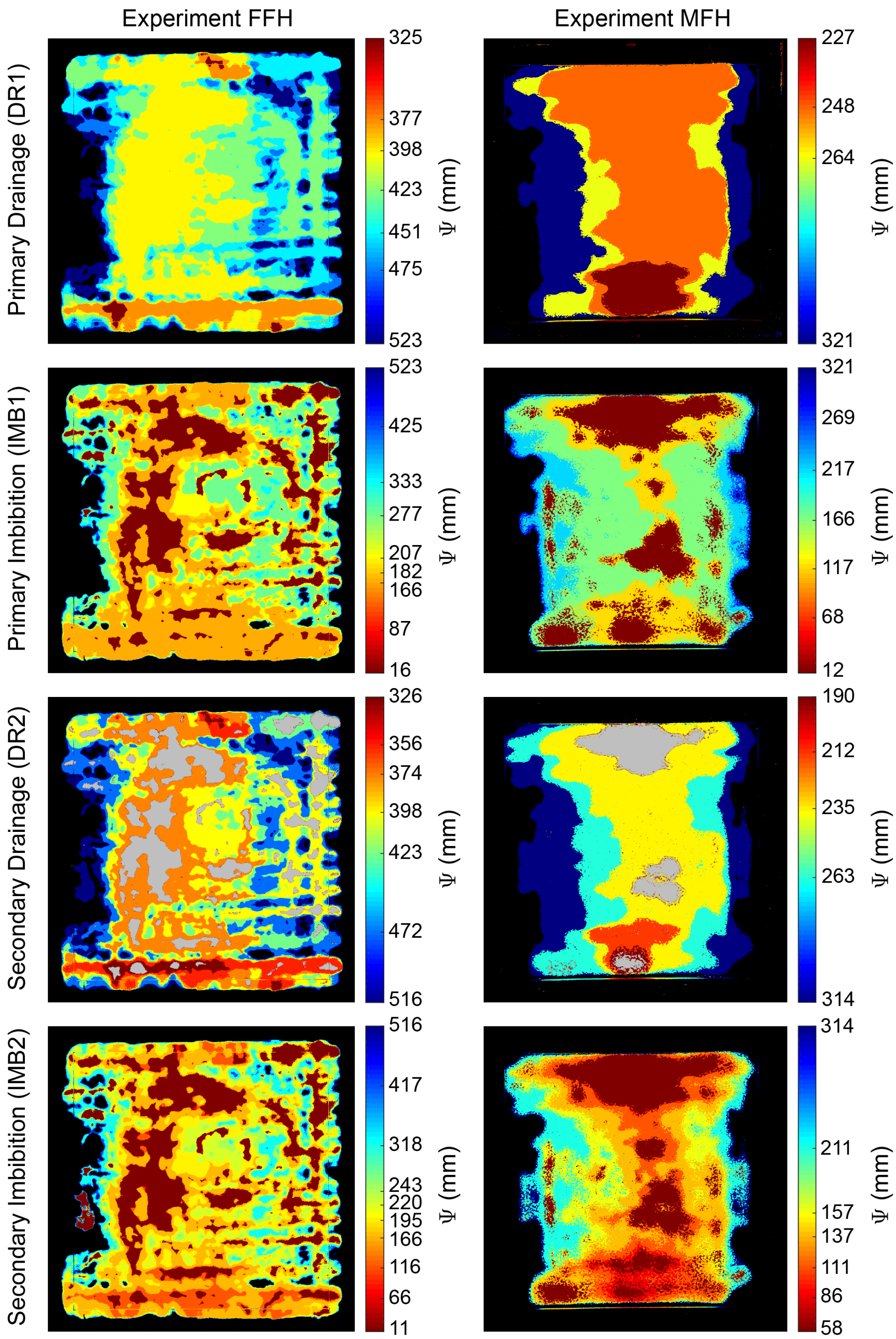

Figure 3. Phase evolution during cyclic drainage and imbibition processes of Experiments FFH and MFH. The average value of the applied capillary head, Ψ, is used to represent each pressure step. Discrete Ψ steps are indicated by the numbers next to the color bar for each sequence and the sequences proceed from top to bottom of each color bar. Warm colors are smaller values of Ψ and cool colors are larger values of Ψ. The color bar range for each drainage cycle begins at the first indication of air entry into the fracture.

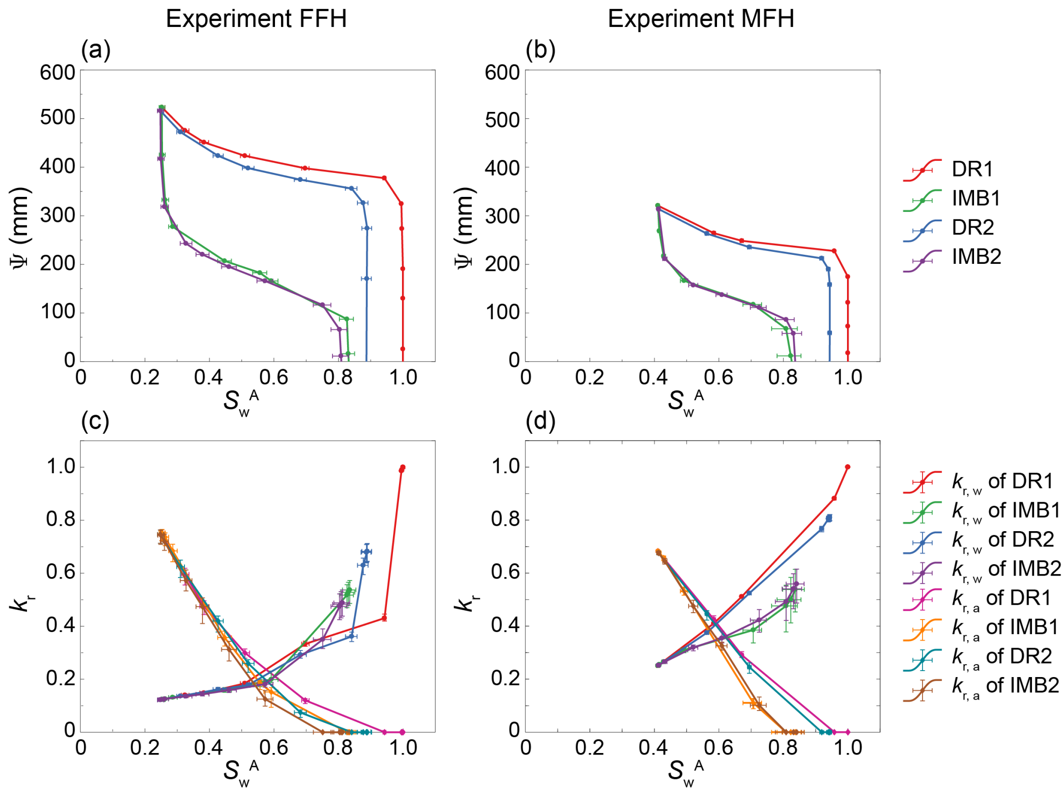

Figure 4. Relationship between applied capillary head Ψ and areal water saturation $S_{\mathrm{w}}^{\mathrm{A}}$ for Experiment FFH (a) and MFH (b), and relationship between modeled relative permeability of water or air ($k_{\mathrm{r,w}}$, $k_{\mathrm{r,a}}$) and areal water saturation $S_{\mathrm{w}}^{\mathrm{A}}$ for Experiment FFH (c) and MFH (d), in which $S_{\mathrm{w}}^{\mathrm{A}}$, $k_{\mathrm{r,w}}$ and $k_{\mathrm{r,a}}$ are the average values during the last 1 min in each step.

Quantitative visualization of two-phase flow in a fractured porous medium

Zhen Liao[1,2], Russell L. Detwiler[3], Esther Cookson[3], Wanjun Lei[1,2], Yi-Feng Chen[1,2]

[1]State Key Laboratory of Water Resources Engineering and Management, Wuhan University, Wuhan 430072, China
[2]Key Laboratory of Rock Mechanics in Hydraulic Structural Engineering of the Ministry of Education, Wuhan University, Wuhan 430072, China
[3]Department of Civil and Environmental Engineering, University of California Irvine, Irvine, CA, United States

Key Points:

- Developed a novel experimental method to visualize two-phase flow in a fracture in a porous matrix.
- The evolution of the air-water distribution within the fracture was measured during sequential drainage and imbibition experiments.
- Capillary head versus saturation curves are sensitive to the pore-size distribution of the bounding porous matrix.

Corresponding author: Russell L. Detwiler, `detwiler@uci.edu`

Abstract

Two-phase fluid flow in fractured porous media impacts many natural and industrial processes but our understanding of flow dynamics in these systems is constrained by difficulties measuring the flow in the interacting fracture and porous media. We present a novel experimental system that allows quantitative visualization of the air and water phases in a single analog fractured porous medium. The fracture system consists of a sintered-glass porous plate in contact with an impermeable glass plate. A reservoir connected to the porous plate allows control of pore pressure within the porous medium. The fracture fills and drains through the porous matrix and flow manifolds along two edges of the fracture. The fracture is mounted in an imaging system that includes a controlled light-emitting diode (LED) panel and a charge-coupled-device (CCD) camera. Flow and pressure are controlled and monitored by a computer during experiments. To demonstrate this system, we carried out a series of cyclic drainage and imbibition experiments in fractures bounded by porous media with different pore-size distributions in the porous matrix. Images of the drainage process demonstrate that the air-water distribution within the fracture evolves differently than has been observed in non-porous fractured systems. Specifically, we observed limited trapping of water within the fracture during drainage. Conversely, during imbibition, because air cannot exit through the porous matrix, significant regions of air became entrapped once pathways to the fracture boundaries became water filled. The differences in phase evolution led to substantial differences in the evolution of estimated relative permeability with saturation.

1 Introduction

Two-phase flow in fractured porous media plays an important role in natural processes such as infiltration into fractured rock and engineered processes such as enhanced oil/gas recovery (Karpyn et al., 2009; Rangel-German & Kovscek, 2002), geological CO_2 sequestration (Vafaie et al., 2023), and remediation of groundwater contaminated by non-aqueous phase liquids (NAPL) (Dearden et al., 2013). Related two-phase flow processes can be broadly categorized as either drainage (non-wetting phase displaces the wetting phase) or imbibition (wetting phase displaces the non-wetting phase).

Early studies of two-phase flow through fractures considered fractures in a non-porous matrix. These studies included experiments in transparent models (e.g., Nicholl et al., 1994; Su et al., 1999) or replicas (e.g., Persoff & Pruess, 1995; Wan et al., 2000) and invasion percolation simulations in variable aperture fields (e.g., Glass et al., 1998; Xu et al., 1998; Yang et al., 2012). In such fractures, flow of the two fluids occurs only through the fracture and the distribution of the phases depends on characteristics of the fracture aperture and the nature and history of the displacement processes. Furthermore, both the wetting and non-wetting fluid may become entrapped and immobilized in regions that are isolated from the fracture boundaries.

When the fractured matrix contains non-negligible porosity, flow of one or both fluids can occur through the fracture and the porous matrix. Two general experimental approaches have been used to study two-phase flow in fractured porous media. The first approach uses micromodels that represent a two-dimensional (2D) cross-section through a fracture; the fracture is a 2D channel and the adjacent porous matrix is a 2D slice of porous medium (e.g., Haghighi et al., 1994; Wan et al., 1996; Rangel-German & Kovscek, 2006). Such experimental systems allow direct visualization of the interaction of multiple phases within the fracture and porous matrix, but neglect the 3D interaction of the phases within the fracture induced by aperture variability.

The second approach combines two-phase flow through cores of fractured porous rock with X-ray computed tomography to observe the distribution of phases within the fracture and porous matrix (Rangel-German & Kovscek, 2002; Karpyn et al., 2009; Arshadi et al., 2018). This has the advantage of providing measurements of the distribution of two or more phases within the pore space (both fracture and porous matrix) in fractured cores. However, the temporal and spatial resolution of CT scans constrains the scalability of these studies. For example, Arshadi et al. (2018) imaged 5-mm segments of a larger fractured core at a 2.5-μm voxel resolution. Such high spatial resolution facilitates identification of phases within pores in the matrix, but limits the size of the fracture that can be imaged.

We developed a novel fractured porous media experimental test cell that consists of a translucent porous glass surface mated with a transparent non-porous glass surface. Quantitative visualization techniques facilitate direct measurement of the evolving phase distribution within the 15$\times$15-cm fracture at a spatial resolution of $\sim$ 75 μm and a temporal resolution of $\sim$ 1 Hz. We demonstrate the new system through a series of drainage and imbibition experiments in fractures with two different pore-size distributions in the porous matrix. We details the experimental system and fabrication of the fracture model in Section 2 ; Section 3 describes the experimental procedure used to demonstrate the results along with the required data analyses; Section 4 presents the results of the demonstration experiments; and Section 5 provides concluding remarks.

2 Experimental System

The experimental system (Figure 1a) includes a test stand that rigidly supports a 12-bit CCD camera (Quantix KAF-6303e; 2048×3072 pixels), red LED backlight panel (with an emitted wavelength of ∼625 nm) and the experimental model. The test stand can rotate from $-90°$ to $90°$ so gravitational forces acting on the fluid in the fracture can be varied. The spatial resolution of images of the fracture plane was 75 × 75 μm. Opaque fabric covers the test stand to minimize stray light in the imaging system. Similar experimental systems have been used to study a range of flow and transport processes in single variable aperture fractures (e.g., Nicholl et al., 1999; Detwiler et al., 1999, 2002)

[Figure 1 about here.]

In this study, we have developed a novel fracture test cell that includes a porous fracture surface. Figure 1b shows a schematic of the fractured porous medium test cell. A porous glass plate (bottom) mated with a smooth glass plate (top) served as the 15×15-cm fracture surfaces. A unique feature of this configuration is that the bottom porous surface is both permeable and translucent, so transmitted light can be measured during experiments. Thus, changes in measured transmitted light intensity reflect the evolving distribution of air and water within the fracture (see Section 3.2 for details). Furthermore, using porous glass with different pore sizes provides the opportunity to directly quantify the influence of matrix porosity and permeability on two-phase flow processes in fractured porous media. The example experiments presented here used two different pieces of porous glass surfaces (Rudong Shundao Glass Instrument Factory, China) with reported pore-size distributions of 4-7 μm (FF - fracture with fine pore-size matrix) and 16-30 μm (MF - fracture with medium pore-size matrix).

Two 1.9-cm-thick fused-quartz windows supported by aluminum frames enclosed the fracture surfaces. Clear polyvinyl chloride (PVC) gaskets separated each fracture surface from the fused-quartz window creating empty cavities between each fracture surface and the supporting window. A needle through the gasket into the lower cavity provided an inlet/outlet for water flow in/out of the porous matrix. To prevent leakage from the edges of the porous lower surface, a rim of dyed epoxy was applied along the peripheral edges of the porous glass (see Text S1, Figure S1 and Figure S2 for additional details).

After placing the smooth glass and the porous glass surfaces in contact to create the fracture, normal stress was applied to the frame by tightening the connecting bolts to a uniform torque (typically 1.7 N·m). Figure 1b shows a rigid frame surrounding the fracture with bolts that apply force to the no-flow boundaries (left and right sides) and flow manifolds (top and bottom). The flow manifold has a $\sim$3 $\times$ 5-mm channel along the entire width of the fracture to ensure that pressure gradients along the manifold channel are negligible relative to pressure gradients within the fracture.

Fluid entered and exited the fracture through tubing connected to the cavity needle and the flow manifolds. For the experiments presented here, a Marriotte bottle connected to the cavity needle served to control the head in the permeable matrix (bottom fracture surface). The Marriotte bottle was positioned on an analytical balance (Mettler Toledo MS4002S/03) on a variable-height stage, which allowed reproducible head changes of up to $\pm$ 70 cm relative to the middle of the fracture plane. We define the capillary head as:

$$\Psi = \frac{p_\mathrm{a} - p_\mathrm{w}}{\rho_\mathrm{w} g} = \frac{p_\mathrm{c}}{\rho_\mathrm{w} g} \tag{1}$$

where p_a, p_w, and p_c are the atmospheric, water, and capillary pressure, respectively, ρ_w is the density of water and g is acceleration due to gravity. During all experiments, a pressure transducer (Validyne DP15-42) monitored p_w at 0.167 Hz. Mass flow rate in and out of the fracture was recorded by the analytical balance. A computer connected to the experimental system controlled data acquisition from each of the sensors (camera, pressure transducer, and balance) using Labview (e.g., Bitter et al., 2006). Manometers adjacent to the pressure transducer facilitated periodic calibration of the pressure transducer but were isolated from the fracture during drainage and imbibition experiments. Because Marriotte bottles lead to small pressure oscillations when bubbles release from the vent tube, we terminated the vent tube with a 16-gauge needle and applied a 0.4 atm vacuum to the head space in the bottle. This caused a steady stream of bubbles from the vent tube and negligible pressure oscillations. To minimize evaporation losses from the Marriotte bottle, we humidified the vent air entering the bottle (Figure 1).

3 Cyclic Drainage and Imbibition Experiments

To demonstrate the capabilities of this new experimental system, we carried out several cyclic drainage and imbibition experiments. Horizontal experiments were carried out in the MF and FF models (Experiments MFH and FFH, respectively) to investigate the effect of the matrix permeability, and one vertical experiment was conducted in FF model (Experiment FFV) to explore the added effect of gravity. Note, results from MFH and FFH are discussed in Section 4; the results of FFV are included in the Supplementary Information (Text SS5).

3.1 Experimental Procedure

Each experimental sequence involved: primary drainage $\rightarrow$ primary imbibition $\rightarrow$ secondary drainage $\rightarrow$ secondary imbibition. Before each experiment, carbon dioxide was injected through the cavity, porous matrix and dry fracture to displace air from the test cell. Then deionized, de-aired water was injected to saturate the fracture. Prior to initializing the first drainage sequence, the boundary conditions for the fracture were established. For the horizontal experiments, the flow manifolds and all connected tubing were drained so the manifolds were filled with air at atmospheric pressure. For the vertical experiment, the top flow manifold and connected tubing were drained, establishing a zero-pressure, air boundary at the top of the fracture, while the bottom manifold and connected tubing were valved off, establishing a no-flow boundary at the bottom of the fracture.

The drainage-imbibition cycles were conducted by sequentially varying the capillary head in the cavity through a set of static displacements of the Marriotte bottle. Image acquisition began before initially changing the position of the Marriotte bottle and continued until the final drainage or imibibition step. During each step, the valve between the cavity and Marriotte bottle (E) was closed as the height of the bottle was adjusted. The valve was then opened and the fracture was allowed to drain or fill until equilibrium. We determined when equilibrium was reached by observing differences between successive raw images and differences between successive mass readings from the digital balance recording the mass of the Marriotte bottle. Each drainage-imbibition cycle was completed during a single day followed by an approximately 12-hour pause before completing the secondary drainage-imbibition cycle.

3.2 Measurement of Evolving Phase Distribution

To aid interpretation of the images acquired during experiments, we developed an image processing script in MATLAB to convert raw images to binary images that distinguished the two phases (air / water). Figure 2 shows the steps of the image processing procedure. At the start of each experiment, we took a sequence of 100 reference images of the saturated matrix and fracture, which we averaged to yield a single, low-noise reference image (Figure 2a). To account for nonuniformities in light transmission through the porous matrix and fracture, we normalized each experimental image (Figure 2b) by the reference image. The natural logarithm of the resulting normalized field quantifies light absorbance at each pixel (Figure 2c).

[Figure 2 about here.]

Light scattering at the interface between the porous matrix and the fracture complicates differentiating air and water within the fracture. Rather than a sharp edge, the air-water interface appears in the absorbance field as a diffuse zone where the values transition from near zero for water to approximately 0.2 for air (Figure 2c). To quantify the location of the interface, we sought a global threshold that minimized the number of air clusters during the primary drainage cycle. The rationale for this approach is that, during primary drainage, we expect the formation of a connected air cluster originating from the fracture inlet with minimal fragmenting of this cluster until the beginning of the subsequent imbibition cycle. Due to noise in the images, smaller threshold values cause localized water-filled regions to be misidentified as air resulting in an increase in the number of air-filled clusters. Larger threshold values cause some thin air-filled channels to be misidentified, separating the large invading cluster into multiple clusters.

To determine the global absorbance threshold, we developed an algorithm that sequentially incremented the threshold over a range that included the likely global threshold value, binarized the field according to each threshold value and counted the resulting number of discrete air clusters. We repeated this process for each image during the primary drainage cycle. Plotting the average number of segmented air clusters, N_{ave}, versus the threshold values for experiments FFH and FFV, T_{FFH} and T_{FFV}, reveals distinct minima for these curves. The respective optimal threshold, $T^{\star}$ for these two experiments were $T^{\star}_{\mathrm{FFH}}$=0.083 and $T^{\star}_{\mathrm{FFV}}$=0.105. We selected a global value of $T^{\star} = 0.094 \pm 0.014$ (average from the two experiments ± 15%) Figure 2d) as the optimal threshold. Figure 2e and f show the results of binarizing using the upper and lower bounds for $T^{\star}$ ($T^{\star}_{\mathrm{lb}} =$ 0.08 and $T^{\star}_{\mathrm{ub}} = 0.108$) and demonstrate that the most significant discrepancies occur where thin tendrils of water (black phase) connect two larger regions of water. We consider the range of possible interface locations as a source of uncertainty in calculations of saturation presented in Section 4. For Experiment MFH, the optimal threshold was $T^{\star}_{\mathrm{MFH}} =$ 0.042 ± 0.006 (Figure S3).

4 Experimental results

Images acquired during each experiment allow us to quantify the evolving phase distribution within the fracture. Figure 3 compares the primary and secondary drainage and imbibition cycles for horizontal experiments in the FF and MF fractures. The colors reflect air occupancy at sequential values of Ψ during each step of the experiment, with warm colors indicating smaller Ψ and cool colors indicating larger Ψ; black regions remained water-filled for all Ψ. The grey regions in the secondary drainage figures are regions that remained air-filled at the end of primary imbibition.

[Figure 3 about here.]

For both experiments, air entered the fracture only after Ψ exceeded the air entry pressure of the fracture ($\Psi_{\mathrm{a,e}}$). Initial air entry occurred after the step from $\Psi = 274$ mm to 325 mm for FFH and after the step from $\Psi = 174$ mm to 190 mm for MFH. The different values of $\Psi_{\mathrm{a,e}}$ reflect differences in the fracture aperture along the two flow boundaries for the two experiments. Though the nonporous glass surface and porous matrix were placed in contact to create the fractures, the size of the sintered beads used to create MF were larger than those used for FF (Figure S4), resulting in a larger aperture and lower $\Psi_{\mathrm{a,e}}$ for MF. The Laplace-Young relationship relates $\Psi_{\mathrm{a,e}}$ to the corresponding fracture apertures (see supporting information Text SS4 and Figure S5 for details) and suggests that the apertures along the flow boundaries are between 43 and 50 μm for FF and between 71 and 77 μm for MF.

The binarized distributions of air and water within the fracture at each increment of Ψ (Figure 3) allow us to quantify the areal fraction of the fracture occupied by water, $S_{\mathrm{w}}^{\mathrm{A}}$. This serves as a surrogate for volumetric water saturation, which we cannot precisely quantify because we have only estimates of the fracture aperture and not aperture variability within the fracture. Figures 4a and 4b show Ψ plotted against $S_{\mathrm{w}}^{\mathrm{A}}$ for each cycle of Experiments FFH and MFH, respectively. The Ψ versus $S_{\mathrm{w}}^{\mathrm{A}}$ plots exhibit significant hysteresis, which can be understood by comparing the phase distributions during different cycles of each experiment.

[Figure 4 about here.]

As primary drainage proceeded through sequential steps of Ψ, air entered regions of progressively smaller aperture. For both FFH and MFH, the air first filled regions near the air-filled flow manifolds and then advanced through the center of the fracture until it connected the two manifolds. Then, with further decreases in Ψ, the region occupied by air expanded towards the no-flow boundaries. The similarity in the large-scale displacement pattern in both experiments likely reflects the influence of the clamping pressure applied to the aluminum frames during fracture assembly (Section 2), which leads to smaller apertures around the perimeter of the fracture. The small-scale features of the displacement patterns differ for the two experiments, likely due to the difference in the porous matrix, which influences the magnitude and variability of fracture aperture and matrix permeability.

A common feature of both experiments is the relative absence of regions of trapped water within the drained region of the fractures (i.e., isolated black regions surrounded by colored regions in Figure 3). This differs from experimental observations in fractures bounded by non-porous, impermeable surfaces, where regions of the draining phase become disconnected from the fracture edges and entrapped within the fracture (e.g., Detwiler et al., 2002; Chen et al., 2017). Here, water regions that become isolated during drainage eventually drain through the porous matrix if the aperture is large enough that Ψ exceeds the local air entry pressure in the fracture.

During primary imbibition, water fills the smallest aperture regions along the no-flow edges of the fractures first and then gradually advances towards the center of the fracture with each increment of Ψ. After water filled the fracture along the two flow manifolds, the remaining air became entrapped and immobilized (dark red regions in second row from top in Figure 3). In contrast to the drainage process, the trapping observed during imbibition is similar to that observed in fractures bounded by non-porous, impermeable surfaces. As a result, potentially large regions of air may become entrapped regardless of the presence of secondary porosity in the bounding porous matrix.

During secondary drainage (DR2) in FFH, air spreads more readily through the fracture than during DR1 due to the regions of trapped air remaining after IMB1. The result is that similar distributions of air and water within the fracture occur at lower values of Ψ during DR2 than DR1. This can be observed in Figure 3 where the distributions of air-filled regions at Ψ=398 mm in DR1 is similar to Ψ=374 mm in DR2. Likewise the distribution of air-filled regions at Ψ=423 mm in DR1 is similar to Ψ=398 mm in DR2. Note, this history dependence is not observed for the imbibition cycles, where the initial distribution of air within the fracture was almost identical for IMB1 and IMB2, resulting in a nearly identical filling order (Figure 3). Similar behavior was observed in MFH, but because the drainage process occurred over a narrower range of Ψ, the differences between DR1 and DR2 are less pronounced.

In addition to the smaller $\Psi_{\mathrm{a,e}}$ during primary drainage for the horizontal experiment in Model MF (Experiment MFH, Figure 4), another significant difference between FFH and MFH was the distribution of the air and water phases during each sequence. Specifically, the air clusters in MFH are more compact with less roughness of the air-water interfaces. Previous scaling analyses of two-phase displacements in fractures between non-porous matrices suggest a reasonable explanation for this behavior (Glass et al., 1998, 2003). The competition between interfacial curvature in the fracture plane and across the fracture aperture have been shown to control the geometry of the air-water interfaces; smaller fracture apertures with more aperture variability lead to more tortuous interfaces than larger aperture fractures with less aperture variability.

Glass et al. (2003) derived the dimensionless parameter, $C/\delta = \frac{\langle b \rangle^2}{\sigma_b \lambda_b}$, where C is the dimensionless curvature number, a ratio of in-plane to out-of-plane interfacial curvature, δ is the coefficient of variation of the fracture aperture, and $\langle b \rangle$, σ_b, and λ_b are the mean, standard deviation, and correlation length of the aperture field. They showed that small C/δ led to tortuous air-water interfaces and as C/δ became larger entrapped regions of air became more compact. Though we cannot directly quantify C/δ for our experiments, the air-entry apertures provide an estimate of $\langle b \rangle$. Because the aperture variability in our fractures are induced by the pore-scale variations of the porous surface, both σ_b and λ_b likely scale with the respective pore sizes of the porous plates. Because the maximum pore sizes for MF are approximately 4 times larger than those in FF, this suggests that C/δ is an order of magnitude larger for MF than for FF. This likely explains the difference in the structure of the air-water interfaces for the two experimental sequences.

It is not possible to directly measure the relative permeability of the air and water phases during our experiments, but we can estimate these values through numerical simulations in the measured air-water distributions. For these simulations, we considered only the influence of the geometry of the air and water on estimated relative permeabilities. Detwiler et al. (2005) showed that the role of aperture variability on estimates of fracture relative permeability were minor relative to the distribution of the flowing phases within the fracture. We used the local cubic law to simulate flow of both air and water through the fracture for each value of Ψ represented in Experiments FFH and MFH. Figures 4c and 4d show the relationship between the estimated water and air relative permeabilities, $k_{\mathrm{r,w}}$ and $k_{\mathrm{r,a}}$, respectively, and the areal saturation $S_{\mathrm{w}}^{\mathrm{A}}$ of the water phase.

The relative permeability curves (Figures 4c and 4d) are qualitatively similar to what has been measured in both porous and fractured media in other studies, suggesting the potential utility of empirical permeability-saturation relationships for modeling flow through fractured porous media. However, the potential for the development of fracture-spanning regions of either air or water can strongly influence the evolution of $k_{\mathrm{r,w}}$. This is most notable in comparing $k_{\mathrm{r,w}}$ during primary and secondary drainage for FFH and MFH. The large region of air that forms at the entrance to FFH (Figure 3) caused a significant decrease in $k_{\mathrm{r,w}}$ once $\Psi_{\mathrm{a,e}}$ was exceeded. Conversely, in MFH, the more compact shape of the evolving air region led to a more gradual decrease in $k_{\mathrm{r,w}}$.

5 Concluding Remarks

We have presented the development and evaluation of a new experimental system for exploring two-phase flow processes in porous fractured media. Use of light transmission through the translucent porous fracture surface allows us to quantitatively delineate the distribution of the evolving air-water interface within the fracture. Example experiments in two different fractures demonstrated the role of changing pore pressure in the porous matrix on the distribution of air and water within the fracture, which exhibited significant hysteresis from the primary drainage through subsequent drainage cycles

The primary advantage of this method over other approaches (e.g., 2D micromodels with a channel bounded by a porous matrix or X-ray CT in rock cores) is the ability to resolve the distribution of air and water within a fractured porous medium at: (i) spatial scales that are much larger than the scale of aperture variability and the resulting regions of entrapped phases during displacement processes; and (ii) temporal scales with the potential to resolve potentially rapidly evolving interfacial dynamics. In addition, the demonstration experiments presented here used a smooth glass plate as the upper fracture surface, but such experiments can be readily extended to include a rough upper fracture surface to explore the relative importance of fracture-matrix interactions and two-phase flow processes within a bounding variable aperture fracture.

6 Open Research

All experimental data and processing algorithms required to reproduce the results presented here are publicly available (Liao et al., 2023).

Acknowledgments

The first author was supported by the scholarship under the State Scholarship Fund from the China Scholarship Council for his visit to University of California, Irvine (CSC student number: 201906270102). We also gratefully acknowledge the financial support from the the Basic Science Center Program for Multiphase Media Evolution in Hypergravity of the National Natural Science Foundation of China (No. 51988101), and the National Natural Science Foundation of China (No. 51925906).

References

Arshadi, M., Khishvand, M., Aghaei, A., Piri, M., & Al-Muntasheri, G. A. (2018). Pore-scale experimental investigation of two-phase flow through fractured porous media. *Water Resources Research*, *54*(5), 3602-3631. doi: https://doi.org/10.1029/2018WR022540

Bitter, R., Mohiuddin, T., & Nawrocki, M. (2006). *Labview: Advanced programming techniques.* CRC Press.

Chen, Y., Fang, S., Wu, D., & Hu, R. (2017). Visualizing and quantifying the crossover from capillary fingering to viscous fingering in a rough fracture. *Water Resources Research*, *53*(9), 7756-7772.

Dearden, R., Noy, D., Lelliott, M., Wilson, R., & Wealthall, G. (2013, oct). Release of contaminants from a heterogeneously fractured low permeability unit underlying a DNAPL source zone. *Journal of Contaminant Hydrology*, *153*, 141–155. doi: 10.1016/j.jconhyd.2011.05.006

Detwiler, R. L., Pringle, S. E., & Glass, R. J. (1999). Measurement of fracture aperture fields using transmitted light: An evaluation of measurement errors and their influence on simulations of flow and transport through a single fracture. *Water Resources Research*, *35*(9), 2605-2617. doi: https://doi.org/10.1029/1999WR900164

Detwiler, R. L., Rajaram, H., & Glass, R. J. (2002). Experimental and simulated solute transport in a partially-saturated, variable-aperture fracture. *Geophysical Research Letters*, *29*(8), 113–1–113–4. doi: https://doi.org/10.1029/2001GL013508

Detwiler, R. L., Rajaram, H., & Glass, R. J. (2005). Satiated relative permeability of variable-aperture fractures. *Physical Review E*, *71*, 031114. doi: https://doi.org/10.1103/PhysRevE.71.031114

Glass, R. J., Nicholl, M. J., & Yarrington, L. (1998). A modified invasion percolation model for low-capillary number immiscible displacements in horizontal rough-walled fractures: Influence of local in-plane curvature. *Water Resources Research*, *34*(12), 3215-3234. doi: https://doi.org/10.1029/98WR02224

Glass, R. J., Rajaram, H., & Detwiler, R. L. (2003). Immiscible displacements in rough-walled fractures: Competition between roughening by random aperture variations and smoothing by in-plane curvature. *Physical Review E*, *68*(6), 061110. doi: https://doi.org/10.1103/PhysRevE.68.061110

Haghighi, M., Xu, B., & Yortsos, Y. C. (1994). Visualization and simulation of immiscible displacement in fractured systems using micromodels: I. Drainage. *Journal of Colloid and Interface Science*, *166*(1), 168-179. doi: https://doi.org/10.1006/jcis.1994.1283

Karpyn, Z. T., Halleck, P. M., & Grader, A. S. (2009). An experimental study of spontaneous imbibition in fractured sandstone with contrasting sedimentary layers. *Journal of Petroleum Science and Engineering*, *67*(1), 48-56. doi: https://doi.org/10.1016/j.petrol.2009.02.014

Liao, Z., Detwiler, R. L., Cookson, E. S., Lei, W., & Chen, Y. (2023). *Dataset for: Quantitative visualization or two-phase flo in a fracture porous medium* [dataset]. doi: 10.5281/zenodo.8188007

Nicholl, M. J., Glass, R. J., & Wheatcraft, S. W. (1994). Gravity-driven infiltration instability in initially dry nonhorizontal fractures. *Water Resources Research*, *30*(9), 2533-2546. doi: https://doi.org/10.1029/94WR00164

Nicholl, M. J., Rajaram, H., Glass, R. J., & Detwiler, R. (1999). Saturated flow in a single fracture: evaluation of the reynolds equation in measured aperture fields. *Water Resources Research*, *35*(11), 3361-3373. doi: https://doi.org/10.1029/1999WR900241

Persoff, P., & Pruess, K. (1995). Two-phase flow visualization and relative permeability measurement in natural rough-walled rock fractures. *Water Resources Research*, *31*(5), 1175-1186. doi: https://doi.org/10.1029/95WR00171

Rangel-German, E. R., & Kovscek, A. R. (2002). Experimental and analytical study of multidimensional imbibition in fractured porous media. *Journal of Petroleum Science and Engineering*, *36*(1), 45-60. doi: https://doi.org/10.1016/S0920-4105(02)00250-4

Rangel-German, E. R., & Kovscek, A. R. (2006). A micromodel investigation of two-phase matrix-fracture transfer mechanisms [Journal Article]. *Water Resources Research*, *42*(3). Retrieved from `https://doi.org/10.1029/2004WR003918` (https://doi.org/10.1029/2004WR003918) doi: https://doi.org/10.1029/2004WR003918

Su, G. W., Geller, J. T., Pruess, K., & Wen, F. (1999). Experimental studies of water seepage and intermittent flow in unsaturated, rough-walled fractures.

Water Resources Research, *35*(4), 1019-1037. doi: https://doi.org/10.1029/1998WR900127

Vafaie, A., Cama, J., Soler, J. M., Kivi, I. R., & Vilarrasa, V. (2023, may). Chemo-hydro-mechanical effects of CO2 injection on reservoir and seal rocks: A review on laboratory experiments. *Renewable and Sustainable Energy Reviews*, *178*, 113270. doi: 10.1016/j.rser.2023.113270

Wan, J., Tokunaga, T. K., Orr, T. R., O'Neill, J., & Connors, R. W. (2000). Glass casts of rock fracture surfaces: A new tool for studying flow and transport. *Water Resources Research*, *36*(1), 355-360. doi: https://doi.org/10.1029/1999WR900289

Wan, J., Tokunaga, T. K., Tsang, C.-F., & Bodvarsson, G. S. (1996). Improved glass micromodel methods for studies of flow and transport in fractured porous media. *Water Resources Research*, *32*(7), 1955-1964. doi: https://doi.org/10.1029/96WR00755

Xu, B., Yortsos, Y. C., & Salin, D. (1998). Invasion percolation with viscous forces. *Physical Review E*, *57*, 739–751. doi: https://doi.org/10.1103/PhysRevE.57.739

Yang, Z., Niemi, A., Fagerlund, F., & Illangasekare, T. (2012). A generalized approach for estimation of in-plane curvature in invasion percolation models for drainage in fractures. *Water Resources Research*, *48*(9), W09507. doi: https://doi.org/10.1029/2012WR011829

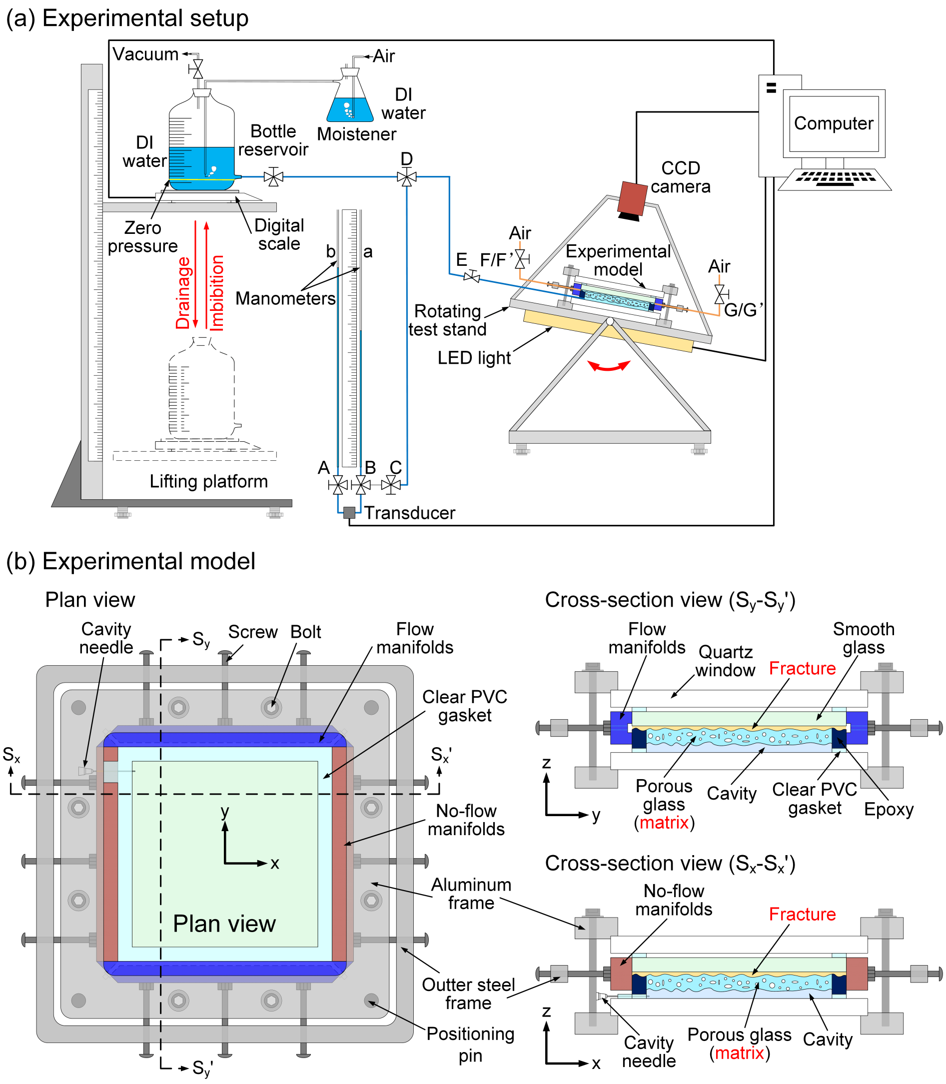

Figure 1. Schematic of experimental system including: (a) an overview of the experimental setup and (b) a plan view and cross-sections of the fracture test cell.

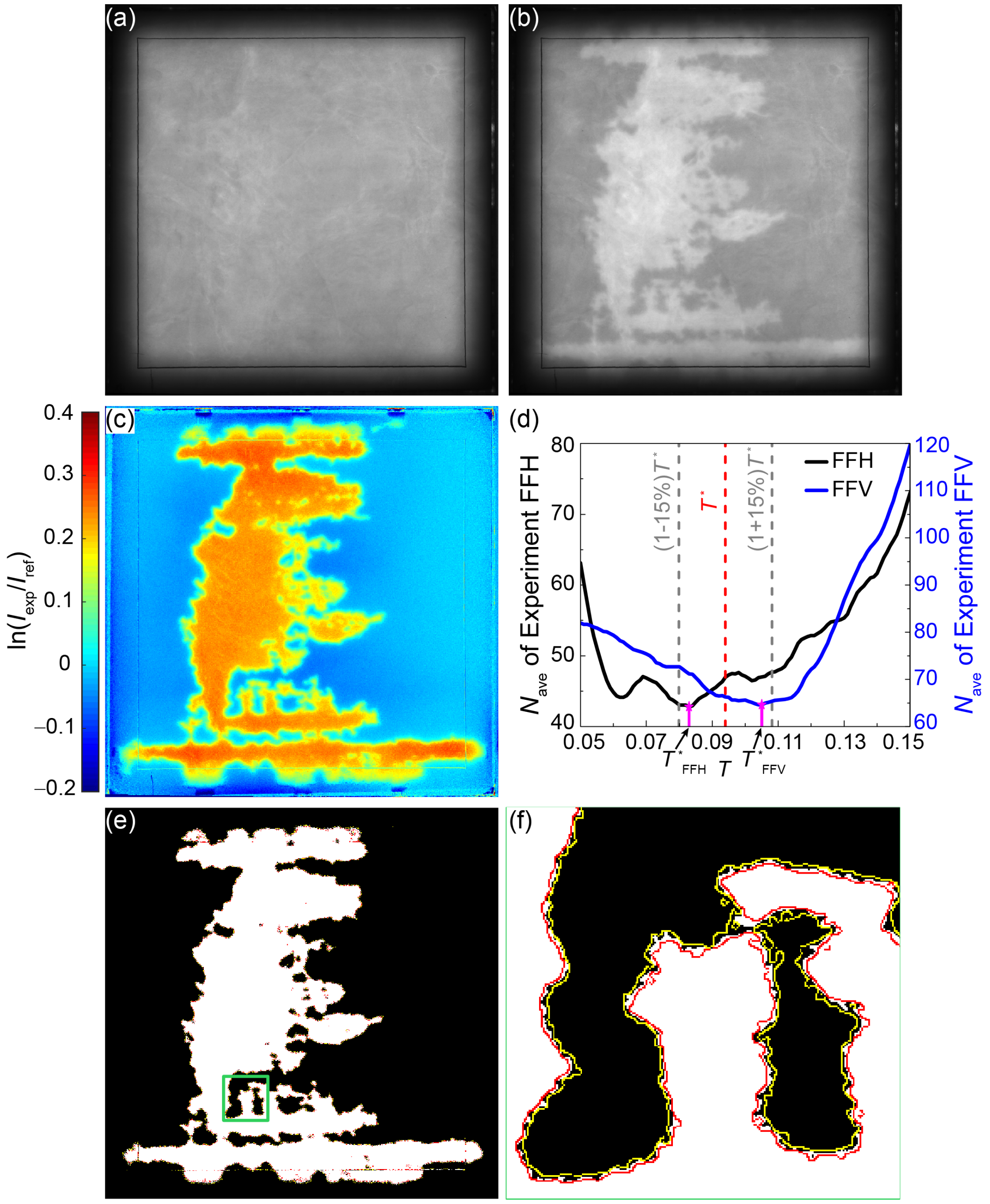

Figure 2. Overview of the image processing procedure, including: (a) The raw grayscale reference image, I_{ref} ; (b) an example of a raw grayscale experimental image, I_{exp}; (c) the corresponding light absorbance field, $A = \ln(I_{\mathrm{exp}}/I_{\mathrm{ref}}$; (d) the relationship between the average number of segmented air clusters, N_{ave}, and the segmenting threshold values for Experiments FFH and FFV, T_{FFH} and T_{FFV}, revealing distinct minima for these curves; (e) the resulting binary image (black - water, white - air) determined using the global threshold with results using the upper and lower bounds of the global threshold indicated by yellow and red lines, respectively; (f) enlarged view of region indicated by the green box in (e).

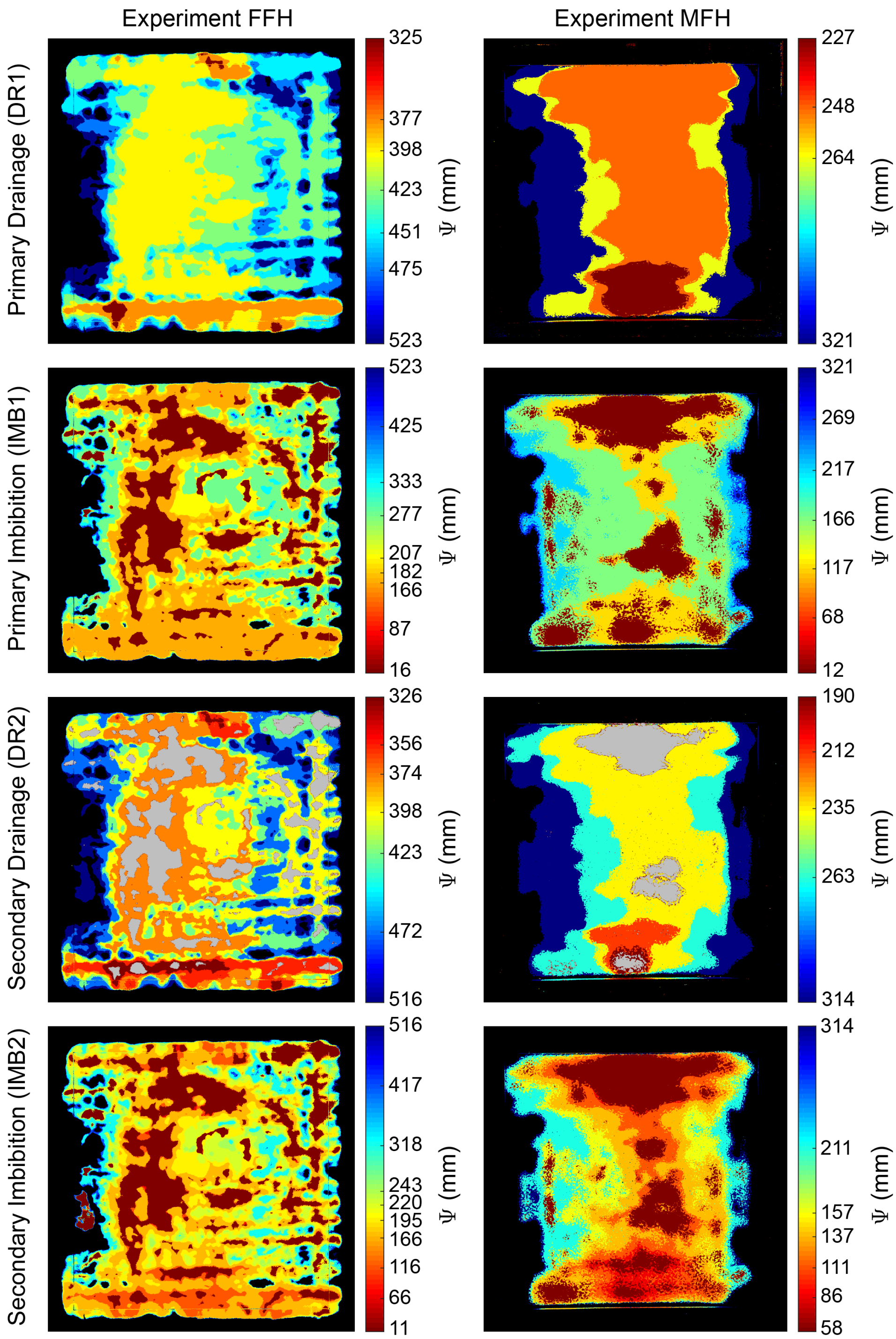

Figure 3. Phase evolution during cyclic drainage and imbibition processes of Experiments FFH and MFH. The average value of the applied capillary head, Ψ, is used to represent each pressure step. Discrete Ψ steps are indicated by the numbers next to the color bar for each sequence and the sequences proceed from top to bottom of each color bar. Warm colors are smaller values of Ψ and cool colors are larger values of Ψ. The color bar range for each drainage cycle begins at the first indication of air entry into the fracture.

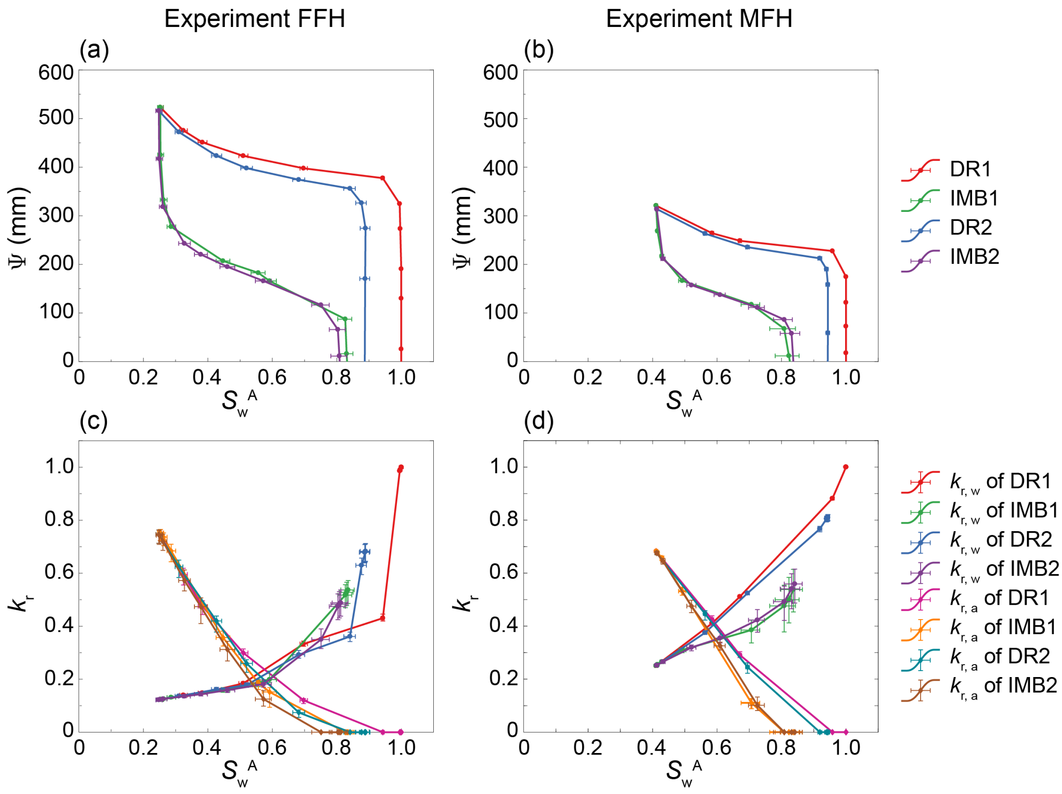

Figure 4. Relationship between applied capillary head Ψ and areal water saturation $S_{\mathrm{w}}^{\mathrm{A}}$ for Experiment FFH (a) and MFH (b), and relationship between modeled relative permeability of water or air ($k_{\mathrm{r,w}}$, $k_{\mathrm{r,a}}$) and areal water saturation $S_{\mathrm{w}}^{\mathrm{A}}$ for Experiment FFH (c) and MFH (d), in which $S_{\mathrm{w}}^{\mathrm{A}}$, $k_{\mathrm{r,w}}$ and $k_{\mathrm{r,a}}$ are the average values during the last 1 min in each step.

Supporting Information for "Quantitative visualization of two-phase flow in a fractured porous medium"

Zhen Liao[1,2], Russell L. Detwiler[3], Esther Cookson[3], Wanjun Lei[1,2], Yi-Feng Chen[1,2]

[1]State Key Laboratory of Water Resources Engineering and Management, Wuhan University, Wuhan 430072, China

[2]Key Laboratory of Rock Mechanics in Hydraulic Structural Engineering of the Ministry of Education, Wuhan University, Wuhan 430072, China

[3]Department of Civil and Environmental Engineering, University of California Irvine, Irvine, CA, United States

Contents of this file

Additional Supporting Information (Files uploaded separately)

1. Movies S1 to S4 show the phase evolution of primary and secondary drainage-imbibition processes in Experiments FFH and MFH, respectively.

Text S1. Procedure of processing the porous glasses.

The square porous glass plates were ordered from Rudong Shundao Glass Instrument Factory, China, and all porous glass plates were processed as follows (Figure S1): (1) Due to the large difference between thickness ($\sim 6\pm1$ mm) and length scale (149 ± 1 mm), a small amount of warping occurred during fabrication inducing a long-wavelength variation. To remove the long-wavelength variation of the porous plates, the top and bottom surfaces were sanded (Norton ProSand 80 secured to a flat glass surface). This process gradually removed sintered glass beads until the surfaces were relatively flat; they retained the small-scale roughness induced by the porosity of the surfaces. After sweeping the powder off the surfaces by a soft brush, the porous glasses were flushed with DI water for several minutes and soaked for 2 hours in DI water with ultrasonication and then dried in a vacuum oven at 45 ℃ overnight. (2) In order to seal the edges and create a cavity, the porous glasses were placed in a specially designed mold, and dyed epoxy was then poured into the mold along the 4 edges. We used West System 105 Epoxy Resin / 206 Slow Hardener. The epoxy penetrated several millimeters into the porous glass to enhance sealing but did not influence the central region of the porous plates (see Figure S2). Note, the epoxy also created a rim surrounding the porous surface that created a cavity between the porous surface and the supporting window when the test cell was assembled. We used Fisher Scientific Sudan Black BP109-10, which is an oily dye that is insoluble in water, to dye the epoxy to facilitate visualization of the epoxy-filled region. After 24 hours of curing at room temperature, the epoxied porous plates were removed from the mold. (3) The epoxy rim surrounding the bottom of each surface were sanded flat and to uniform thickness using P80 sandpaper and then polished using P400 sandpaper.

The resulting smooth bottom surface ensured water-tight contact with the bottom PVC gasket to prevent leakage. The 4 edges of the epoxied porous glasses were then sanded to match the size of the smooth glass surface, which ensured the porous surface mated well with the smooth glass to simplify sealing of the no-flow boundaries and flow manifolds. The epoxied and sanded porous plates were then cleaned and dried again through the same cleaning and drying process. Finally, the epoxied regions around the edges of the porous surfaces were smoother than the un-epoxied regions because the pores were filled with epoxy. This resulted in very small fracture apertures around the perimeter of the fracture when the test cell was assembled. To provide a pathway for air to enter the central region of the fracture, we created 3 wedge-shaped grooves equally distributed along the sides of the fractures connected to the flow manifolds (Figure S2). This allowed us to focus on the flow in the central fracture, where the matrix porosity is unaffected by epoxy and boundary constraints.

Text S2. Aperture estimation based on Laplace-Young relationship.

For a two-phase flow in fracture, we know that the capillary head (Ψ) is a function of the principal radii of curvature and the interfacial tension according to the Laplace-Young equation (Glass et al., 1998):

$$\Psi = \frac{\gamma}{\rho_{\mathrm{w}} g}\left(\frac{1}{r_1} + \frac{1}{r_2}\right) \tag{S1}$$

where γ is the interfacial tension, r_1 is the radius of aperture-induced curvature and r_2 is the radius of in-plane curvature. By assuming that the fracture walls are symmetric about a mean plane and neglecting the influence of local convergence/divergence angle (β) of the fracture walls, r_1 can be calculated as (Yang et al., 2012):

$$r_1 = \frac{b}{2\cos\theta} \tag{S2}$$

where b is the fracture local aperture, and θ is the contact angle of the fluid-fluid-fracture system. Actually, another assumption underlying equation (S2) is that the contact angle θ is the same on the top and bottom fracture surfaces. While in our experimental model, we noticed that the contact angle on the smooth glass and the porous glass (FF or MF) are not exactly the same (Figure S5 (a)), thus equation (S2) should be modified as follows (see Figure S5 (b)):

$$r_1 = \frac{b}{\cos\theta_1 + \cos\theta_2} \tag{S3}$$

in which θ_1 and θ_2 are the contact angle of water and air on the smooth glass and the porous glass, respectively, and their measured value are shown in Figure S5 (a).

What's more, the influence of r_2 is often assumed to be negligible (i.e., r_2 is much larger than r_1) (Glass et al., 1998), therefore the capillary head Ψ can be approximated as:

$$\Psi = \frac{\gamma(\cos\theta_1 + \cos\theta_2)}{\rho_{\mathrm{w}} g b} \tag{S4}$$

Or the local fracture aperture b can be estimated by the applied capillary head Ψ:

$$b = \frac{\gamma(\cos\theta_1 + \cos\theta_2)}{\rho_{\mathrm{w}} g \Psi} \tag{S5}$$

Text S3. Results of Experiment FFV

In order to investigate how gravity affects the cyclic drainage and imbibition processes, the vertical experiment (Experiment FFV) was conducted in the same FF fractures. Phase distributions at the end of each pressure step are shown in Figure S6, in which the capillary head Ψ was defined relative to the fracture's centerline. Because the bottom manifold and connected tubing were closed off, the air can only invade into the fracture through the top edge during the primary drainage process. Rather than a relatively uniform capillary head Ψ applied to the horizontal fracture in Experiment FFH, the Ψ applied to the vertical fracture actually distributed linearly along the fracture length (from Ψ to Ψ-152 mm). This linear distribution suppressed the air to vertically invade into the lower part of the fracture when $\Psi \leq 426$ mm, as the actual capillary head applied to the lower part of the fracture is not big enough to overcome the capillary pressure. However, the water has a potential tendency to flow downward under its own gravity, thus facilitating the air to spread to the no-flow boundaries, resulting a wider invasion front than Experiment FFH. An intuitive understanding of this difference can be gained by comparing the air cluster pattern at step Ψ=401 mm in primary drainage (DR1) of Experiment FFV with step Ψ=398 mm in DR1 of Experiment FFH. As the Ψ continues to increase, the air finally breaks through the bottom edge of the fracture and invades the bottom manifold, causing some water that existed in the bottom manifold to be imbibed into the fracture and flow into the reservoir through the matrix. After that, with further increases in Ψ, air expanded towards the no-flow boundaries. During the imbibition processes, due to the effect of the gravity of water and the buoyancy of air, the air became relatively easy to displaced out from the top edge, thus less air was trapped in the lower part of the fracture, and the overall residual air saturation at the end of the imbibition processes was lower than that in Experiment FFH.

Figure S7a shows Ψ plotted against $S_{\mathrm{w}}^{\mathrm{A}}$ for each cycle of Experiment FFV, which also exhibits significant hysteresis. Figure S7b shows the relationship between the estimated water and air relative permeabilities, $k_{\mathrm{r,w}}$ and $k_{\mathrm{r,a}}$, respectively, and the areal saturation $S_{\mathrm{w}}^{\mathrm{A}}$ of the water phase. By comparing the air relative permeability $k_{\mathrm{r,a}}$ of FFV with FFH, one can intuitively find that air is less permeable due to the effect of gravity, i.e., air is permeable ($k_{\mathrm{r,a}} > 0$) when $S_{\mathrm{w}}^{\mathrm{A}}$ is less than ~ 0.5 in Experiment FFV, while in FFH, air is permeable when $S_{\mathrm{w}}^{\mathrm{A}}$ is less than ~ 0.7.

Movie S1. Phase evolution of primary drainage and imbibition process in Experiment FFH.

Movie S2. Phase evolution of secondary drainage and imbibition process in Experiment FFH.

Movie S3. Phase evolution of primary drainage and imbibition process in Experiment MFH.

Movie S4. Phase evolution of secondary drainage and imbibition process in Experiment MFH.

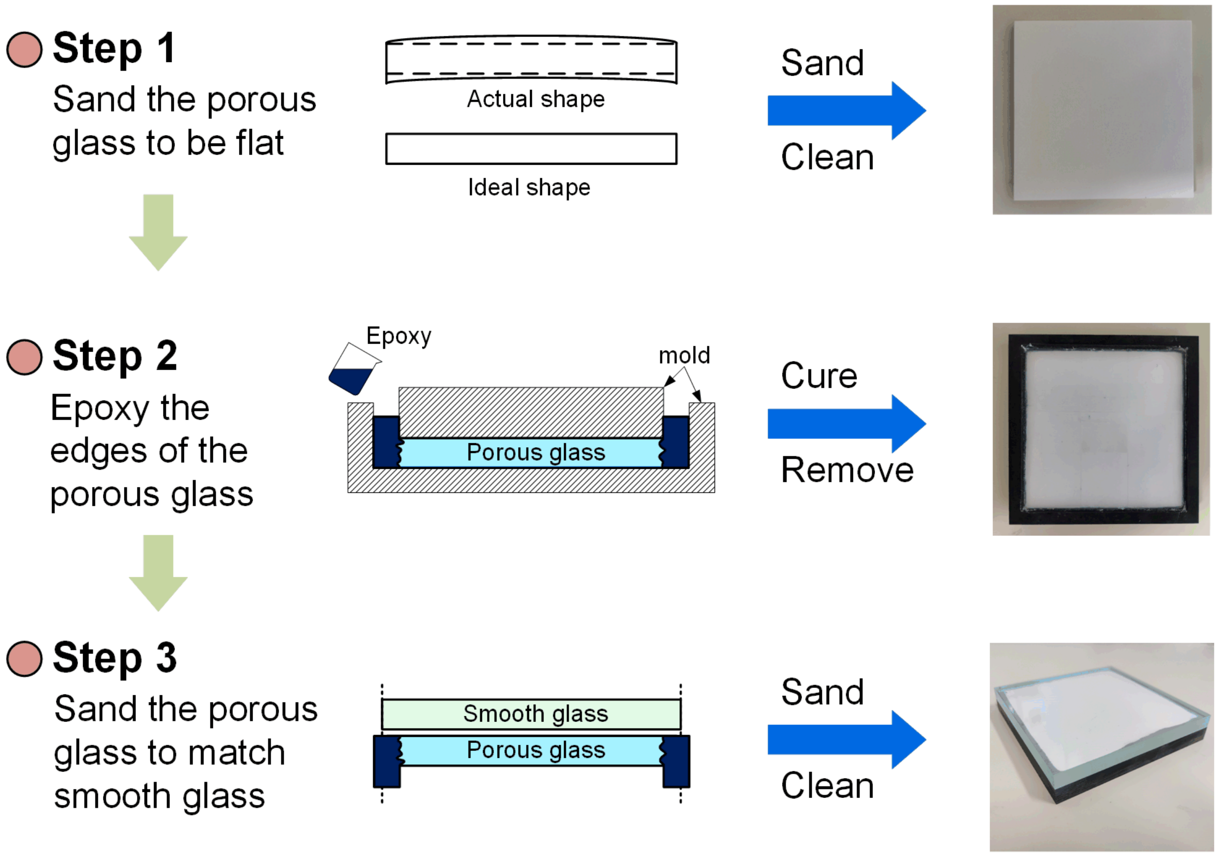

Figure S1. The procedure of processing the porous glasses.

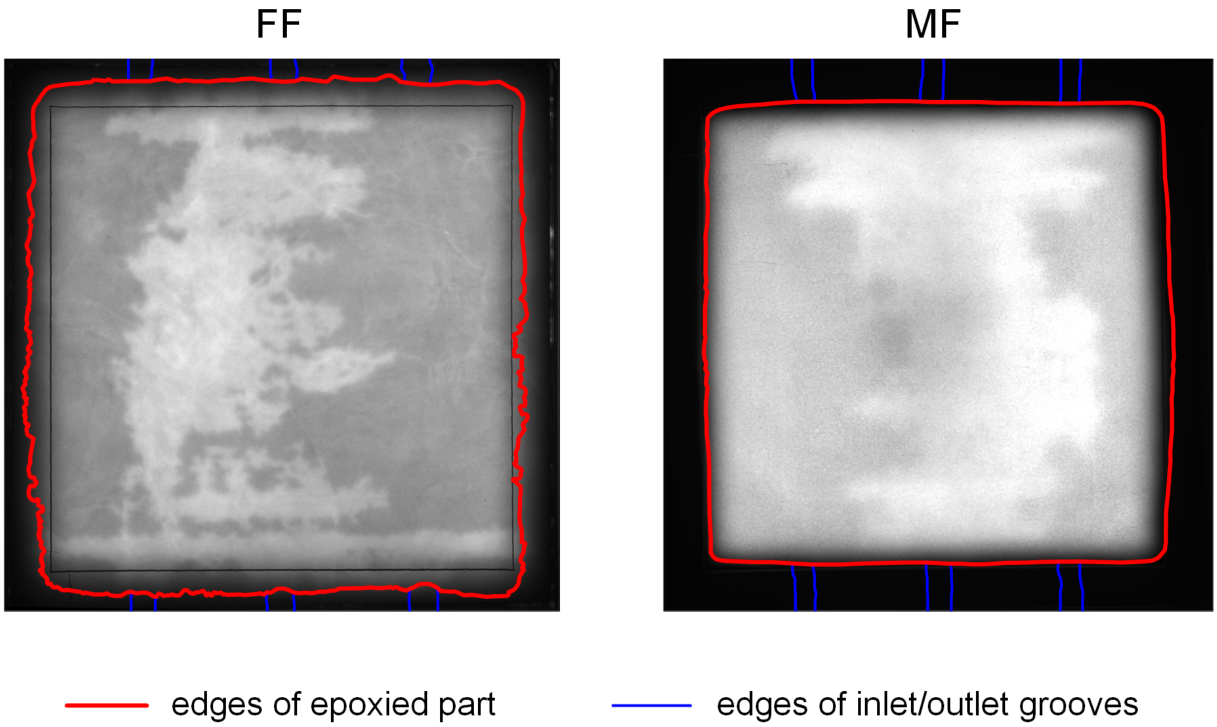

Figure S2. Edges of the epoxied part and inlet/outlet grooves of the FF and MF model. The ratios of projected area of the epoxied part to the projected area of the porous glass's top surface are about 18.59% and 30.15% for FF and MF model, respectively. The background raw images are corresponding to the end of the pressure steps at $\Psi = 398$ and 248 mm for FF and MF model, respectively.

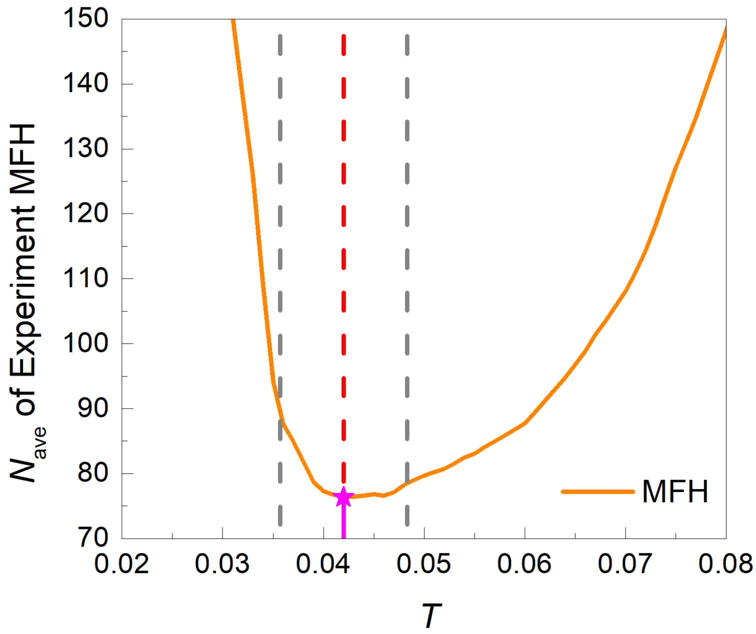

Figure S3. The N_{ave}-T plot of Experiment MFH. Plotting the average number of segmented air clusters, N_{ave}, versus the threshold values for Experiment MFH, T_{MFH}, also reveals distinct minima. The optimal threshold was $T^{\star}_{\mathrm{MFH}} = 0.042 \pm 0.006$.

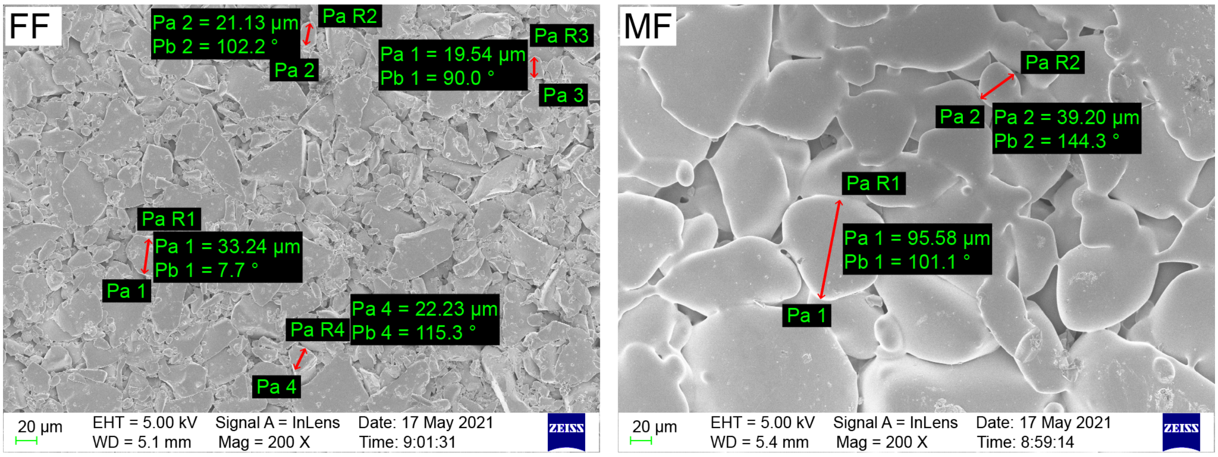

Figure S4. SEM images of the porous glasses. High resolution images of the surfaces of FF (fracture with fine pore-size matrix) and MF (fracture with medium pore-size matrix), captured by the field emission scanning electron microscopy (SEM) in Wuhan University, showing big difference of the sintered bead sizes between FF and MF.

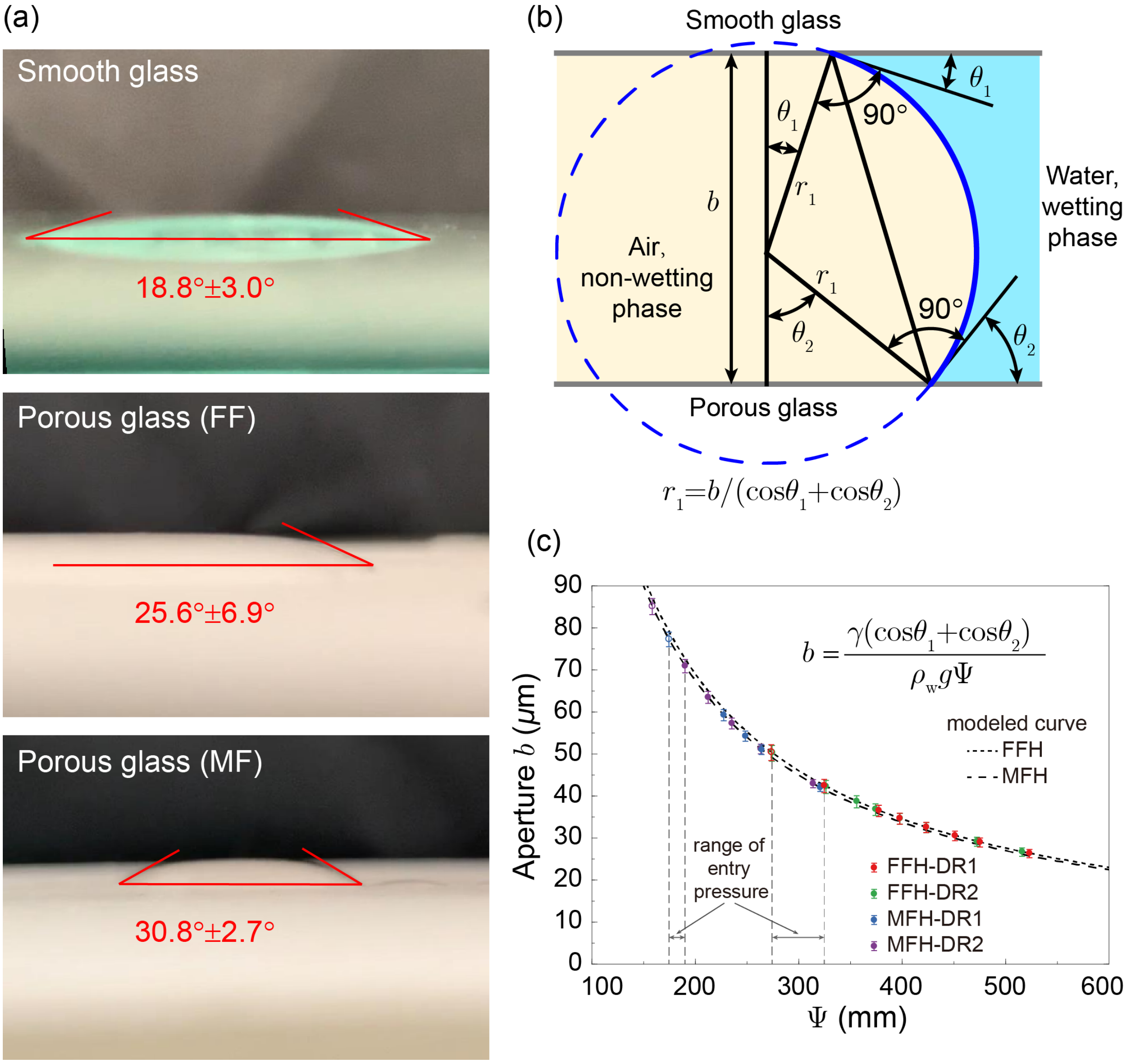

Figure S5. Aperture estimation based on Laplace-Young relationship. (a) Measured contact angles on the smooth glass and porous glass. (b) Cross-section illustration of a water-air interface within the fracture, showing the radius of aperture-induced curvature r_1 related to the fracture local aperture b and different contact angles on the smooth glass and porous glass (θ_1 and θ_2). (c) Estimated fracture local aperture b corresponding to the applied capillary head Ψ based on equation (S4) (modeled curves), in which the hollow and solid circles represent the experimental steps that air didn't invade or invaded into the fracture.

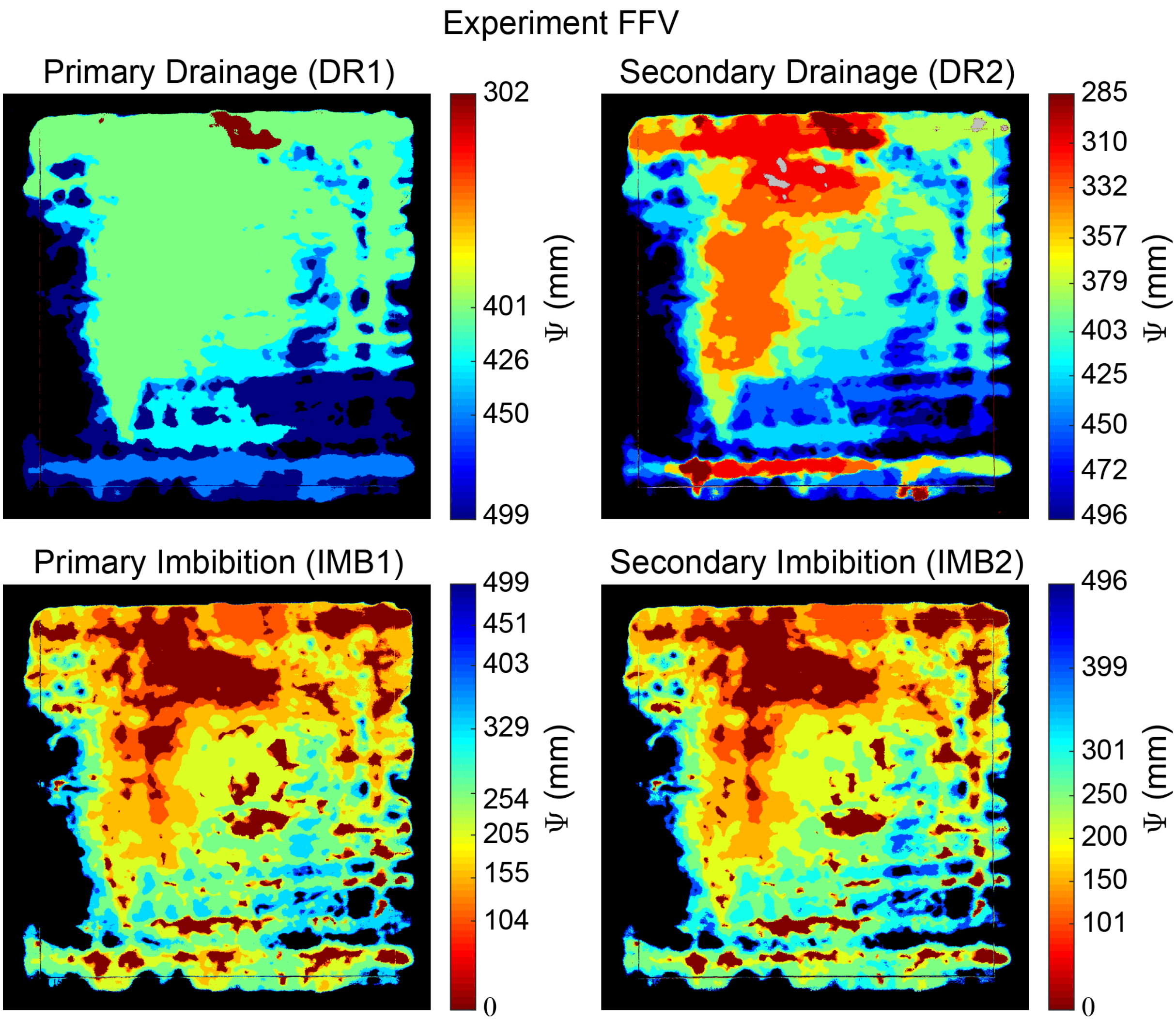

Figure S6. Phase evolution during cyclic drainage and imbibition processes of Experiment FFV. The colors reflect air occupancy at sequential values of Ψ during each step of the experiment, with warm colors indicating smaller values of Ψ and cool colors indicating larger Ψ; black regions remained water-filled at the breakthrough Ψ (final step of each experiment). The grey regions in the secondary drainage figures are regions that remained air-filled at the end of primary imbibition.

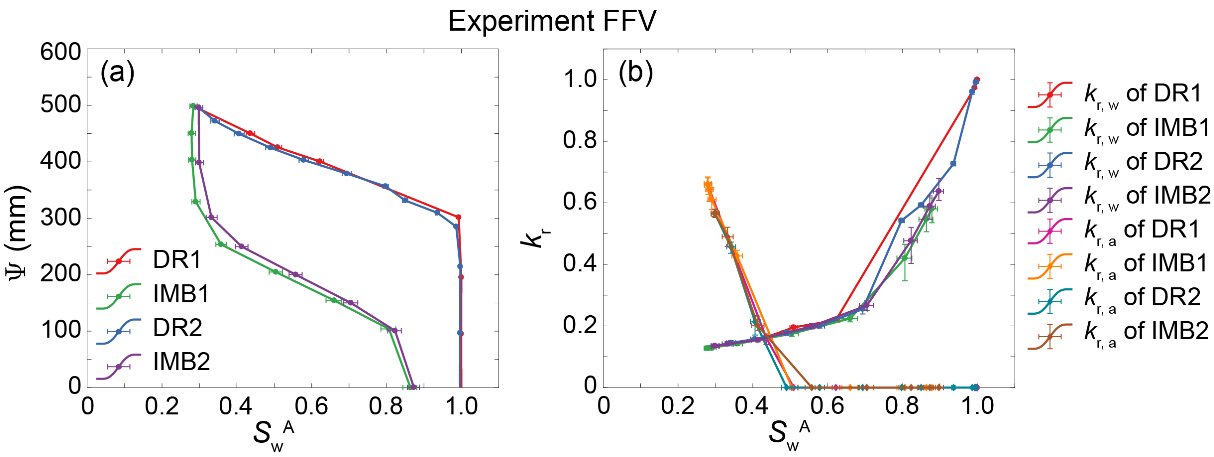

Figure S7. Relationship between applied capillary head Ψ and areal water saturation $S_{\mathrm{w}}^{\mathrm{A}}$ for Experiment FFV (a), and relationship between modeled relative permeability of water or air ($k_{\mathrm{r,w}}$, $k_{\mathrm{r,a}}$) and areal water saturation $S_{\mathrm{w}}^{\mathrm{A}}$ for Experiment FFV (b), in which $S_{\mathrm{w}}^{\mathrm{A}}$, $k_{\mathrm{r,w}}$ and $k_{\mathrm{r,a}}$ are the average values during the last 1 min in each step.

References

Glass, R. J., Nicholl, M. J., & Yarrington, L. (1998). A modified invasion percolation model for low-capillary number immiscible displacements in horizontal rough-walled fractures: Influence of local in-plane curvature. *Water Resources Research*, *34*(12), 3215-3234. doi: https://doi.org/10.1029/98WR02224

Yang, Z., Niemi, A., Fagerlund, F., & Illangasekare, T. (2012). A generalized approach for estimation of in-plane curvature in invasion percolation models for drainage in fractures. *Water Resources Research*, *48*(9), W09507. doi: https://doi.org/10.1029/2012WR011829